

This is a postprint version of the following published document:

Gallo, A., Alonso, E., Pérez-Rábago, C., Fuentealba, E., & Roldán, M. I. (2019). A lab-scale rotary kiln for thermal treatment of particulate materials under high concentrated solar radiation: Experimental assessment and transient numerical modeling. *In Solar Energy*, 188, 1013–1030

DOI: [10.1016/j.solener.2019.07.006](https://doi.org/10.1016/j.solener.2019.07.006)

© 2019 International Solar Energy Society. Published by Elsevier Ltd.  
All rights reserved.



This work is licensed under a [Creative Commons Attribution-NonCommercial-NoDerivatives 4.0 International License](https://creativecommons.org/licenses/by-nc-nd/4.0/).

# 1 A lab-scale rotary kiln for thermal treatment of 2 particulate materials under high concentrated solar 3 radiation: experimental assessment and transient 4 numerical modeling

5 Alessandro Gallo<sup>a,b,\*</sup>, Elisa Alonso<sup>a</sup>, Carlos Pérez-Rábago<sup>c</sup>, Edward Fuentealba<sup>a</sup> and María Isabel  
6 Roldán<sup>b</sup>

7 <sup>a</sup>Energy Development Center of Antofagasta. University of Antofagasta (Chile)

8 <sup>b</sup>Doctorado en “Ciencias Aplicadas al Medio Ambiente” (RD99/11). University of Almeria (Spain)

9 <sup>c</sup>Institute of Renewable Energies. National Autonomous University of Mexico (Mexico)

10 \*Corresponding author: alessandro.gallo@uantof.cl;

11 **Abstract:** Rotary kilns are worldwide used for industrial processes that involve thermal treatments  
12 of particulate materials. However, a great amount of fossil fuels is employed in such processes. As  
13 alternative, solar rotary kilns are considered for this application due to their versatility and potential  
14 to substitute traditional fossil-fuel driven devices. In order to boost the development of this  
15 technology, efforts have to be focused on the control of the particle temperature during the  
16 treatment. In this context, a lab-scale rotary kiln was built and tested using a 7-kW<sub>e</sub> high-flux solar  
17 simulator at University of Antofagasta. It was conceived to treat particulate materials of different  
18 nature and it is able to reach temperatures higher than 800 °C under different operation strategies.  
19 Silicon carbide was selected for initial tests because it is inert, endures high temperatures (up to 1600  
20 °C) and it has been proposed as thermal storage vector in several researches on concentrated solar  
21 power. In a first stage, the empty kiln was preheated up to about 800 °C, reaching a steady state in  
22 less than three hours and with a power of approximately 370 W entering the kiln cavity. Afterwards,  
23 43 g of silicon carbide were introduced in the furnace and the system was heated again up to a  
24 second steady state above 800 °C. In this stage, particles showed a fast increment of their  
25 temperature and exceeded 700 °C in less than three minutes after loading. A one-dimensional  
26 transient numerical model was also developed to perform the thermal analysis of the kiln and the  
27 estimation of both the particle temperature and the system efficiency. Numerical results showed  
28 good agreement with experimental data and thermal losses could be quantified in detail. Therefore,  
29 the model was also used to predict the thermal behavior of a solar rotary kiln working in batch  
30 mode.

31 **Keywords:** Concentrating solar heat, rotary kilns, industrial applications, solar thermal receiver  
32

---

## 33 NOMENCLATURE

Notation

|             |  |
|-------------|--|
| $A$         | area of surface, (m <sup>2</sup> )   |
| $Bi$        | Biot number, (-)   |
| $c$         | chord length of circular segment, (m)  |
| $cp$        | specific heat, (J kg <sup>-1</sup> K <sup>-1</sup> )   |
| $D$         | diameter, (m)  |
| $E$         | total emissive power or radiant flux of a black body: rate of radiant energy emitted by a surface in all directions per unit area of the surface, (W m <sup>-2</sup> ) |
| $En$        | thermal energy, (Wh)   |
| $ER_{50\%}$ | median relative error, (%)   |
| $F_{x-y}$   | view factor from surface x to surface y, (-)   |

|                         |  |
|-------------------------|--|
| $f$                     | correction factor, (-)   |
| $FR\%$                  | fill ratio or degree of fill, (%)  |
| $Fr$                    | Froude number, (-)   |
| $g$                     | gravity acceleration, ( $= 9.81 \text{ m s}^{-2}$ )  |
| $Gr$                    | Grashof number, (-)  |
| $h$                     | height of particle bed, (m)  |
| $h_x$ or $h_y^x$        | heat transfer coefficient for x component and y mechanism, $\text{W m}^{-2} \text{K}^{-1}$   |
| $J$                     | radiosity or radiant exitance: radiant flux leaving a surface per unit area as sum of emitted and reflected radiation, ( $\text{W m}^{-2}$ ) |
| $K$                     | conductivity, ( $\text{W m}^{-1} \text{K}^{-1}$ )  |
| $L$                     | kiln length, (m)   |
| $Lc$                    | characteristic length, (m)   |
| $m$                     | mass, (kg)   |
| $M$                     | Maxwell equation   |
| $n$                     | total time steps, (-)  |
| $N$                     | rotational speed, (rpm)  |
| $Nu$                    | Nusselt number, (-)  |
| $q$                     | thermal power per unit area, ( $\text{W m}^{-2}$ )   |
| $Q$                     | thermal power, (W)   |
| $R$                     | radius, (m)  |
| $s$                     | slope of the kiln, (degree)  |
| $t$                     | time, (s)  |
| $T$                     | temperature, (K)   |
| $TR$                    | thermal resistance, ( $\text{K W}^{-1}$ )  |
| $V$                     | volume, ( $\text{m}^3$ )   |
| $v_{rot}$               | speed at inner wall of cavity, ( $\text{m s}^{-1}$ )   |
| Greek letters           |  |
| $\alpha$                | thermal diffusivity, ( $\text{m}^2 \text{s}^{-1}$ )  |
| $\beta$                 | coefficient of volumetric expansion, ( $\text{K}^{-1}$ )   |
| $\varepsilon$           | emissivity, (-)  |
| $\theta$                | central angle, (rad)   |
| $\rho$                  | density, ( $\text{kg m}^{-3}$ )  |
| $\sigma$                | Stefan-Boltzmann constant ( $= 5.67 \cdot 10^{-8} \text{ W m}^{-2} \text{K}^{-4}$ )  |
| $\tau$                  | contact time, (s)  |
| $\varphi$               | volume fraction or porosity, (-)   |
| $\omega$                | angular speed, ( $\text{rad s}^{-1}$ )   |
| Subscripts/Superscripts |  |
| <i>air</i>              | air  |
| <i>amb</i>              | ambient  |
| <i>ap</i>               | aperture of cavity   |
| <i>b</i>                | particle bed or bulk   |
| <i>cav</i>              | cavity   |
| <i>cb</i>               | covered bed  |
| <i>cd</i>               | conduction   |
| <i>cv</i>               | convection   |
| <i>cw</i>               | covered wall   |
| <i>e</i>                | electrical   |
| <i>end</i>              | final point  |
| <i>env</i>              | envelope   |
| <i>ext</i>              | external   |
| <i>exp</i>              | experimental   |
| <i>fc</i>               | forced convection  |

|                                |   |
|--------------------------------|---|
| <i>i</i>                       | <i>i</i> -th control volume   |
| <i>ins</i>                     | insulation  |
| <i>j</i>                       | <i>j</i> -th element  |
| <i>H</i>                       | heating   |
| <i>in</i>                      | inlet   |
| <i>L</i>                       | loading   |
| <i>l</i>                       | losses  |
| <i>max</i>                     | maximum   |
| <i>nc</i>                      | natural convection  |
| <i>net</i>                     | net   |
| <i>p</i>                       | particle  |
| <i>PH</i>                      | pre-heating   |
| <i>proc</i>                    | process   |
| <i>rad</i>                     | radiation   |
| <i>rad-out</i>                 | exiting radiation from the aperture   |
| <i>ref</i>                     | reference   |
| <i>refl</i>                    | reflective  |
| <i>rel</i>                     | relative  |
| <i>sim</i>                     | simulated   |
| <i>steel</i>                   | steel of casing and rotor   |
| <i>t</i>                       | <i>t</i> -th instant  |
| <i>tr</i>                      | transversal   |
| <i>w</i>                       | crucible wall   |
| <i>0</i>                       | starting point  |
| Acronyms                       |   |
| Al <sub>2</sub> O <sub>3</sub> | aluminum oxide (alumina)  |
| CCD                            | Charge Coupled Device   |
| CNRS                           | national center of scientific research (Centre National de la Recherche Scientifique)   |
| CSE / CSP                      | Concentrated Solar Energy / Power   |
| EMT                            | Effective Medium Theory   |
| HFSS                           | High Flux Solar Simulator   |
| HoSIER                         | IER solar furnace (Horno Solar del IER)   |
| GHG                            | Green-House Gases   |
| IER                            | renewable energy institute (Instituto de Energías Renovables)   |
| IEA                            | International Energy Agency   |
| LaCoSA                         | solar concentration laboratory of university of Antofagasta (Laboratorio de Concentración Solar de la Universidad de Antofagasta) |
| MAPE                           | Mean Absolute Percentage Error  |
| ND                             | Neutral Density   |
| RMSE                           | Root Mean Square Error  |
| SiC                            | Silicon Carbide   |
| SPSR                           | Solid Particle Solar Receiver   |
| UARR                           | University of Antofagasta Rotary Receiver   |
| UNAM                           | national autonomous university of Mexico (Universidad Nacional Autónoma de México)  |

## 36 1. Introduction

37 Rotary kilns have a long tradition of use in several industrial sectors such as casting, drying  
38 materials, cement production, food industry, etc. This technology is suitable for the mixing of  
39 granular materials and, in thermal treatments, it is possible to achieve a homogeneous temperature  
40 distribution in the particle bed of the kiln. Thus, these devices can act as driers, heaters, or chemical  
41 reactors (Boateng, 2008). Moreover, rotary kilns are versatile: they can work with materials of  
42 different size and shape, either powder or particles, and can operate in a huge range of temperature,  
43 from ambient to more than 2000 °C. They also have low costs of maintenance and long-life  
44 components. However, these devices are normally fed with fossil fuels and due to their intensive use  
45 in the industry they have a high environmental impact (Alonso et al., 2017a).

46 To clean and reduce the impact of these kilns, several researches have been focused in replacing  
47 fossil fuels with concentrated solar energy. Although these solar rotary kilns have not reached the  
48 commercial maturity, they were proposed with satisfactory results for different applications such as  
49 dangerous waste treatment (Funken et al., 1999), lime production (Meier et al., 2006, 2004), or  
50 aluminum recycling (Alexopoulos et al., 2015). Another innovative application consisted in the  
51 reduction of metal oxides in the first stage of the production of solar fuels (Abanades et al., 2007;  
52 Kaneko et al., 2007; Koepf et al., 2016; Schunk and Steinfeld, 2009). All of these kilns were studied in  
53 a lab or pilot scale coupled with solar furnaces or solar simulators for experimental demonstrations  
54 (Alonso et al., 2017a).

55 Over the last years, the storage of thermal or thermochemical heat in solid particles has emerged  
56 as application of the concentrating solar technologies and different kinds of receiver have been  
57 developed. Depending on the material used, these particles may be cheaper, and they can work at  
58 higher temperatures than other heat transfer fluids (i.e. molten salt, water, thermal oils) (Alonso and  
59 Romero, 2015; Gallo et al., 2015; Ho, 2017). Therefore, rotary drums were proposed as candidates for  
60 such solar receivers (Alonso et al., 2017b, 2015; Gallo et al., 2018; Koepf et al., 2016; Neises et al., 2012;  
61 Sammouda et al., 1999).

62 Despite the numerous researches on these devices, not many numerical models have been  
63 conducted on solar rotary kilns. This is probably due to the great variety of kilns, treated materials  
64 and operational modes, that need specific models for each analyzed case. One of this model was  
65 carried out by Schunk et al. (2009). They validated with experimental texts a transient CFD heat  
66 transfer model of a solar receiver-reactor for thermal dissociation of ZnO and then scaled the reactor  
67 up to 1 MW. The kiln worked in semi-batch mode at high speed (30 - 120 rpm), presumably in  
68 centrifugal mode, and the particles covered the entire inner surface of the crucible. They found a  
69 maximum uniform superficial temperature of about 1800 °C in the ZnO layer.

70 In the case of Alexopoulos et al. (2015), they carried out a mathematical model for the simulation  
71 of the unsteady behavior of a solar heated rotary kiln for aluminum recycling. The kiln was fed in  
72 batch mode with aluminum and salt. In the cavity, convection was forced by the suction of the  
73 exhaust gas. The model was validated with experimental results in a pilot plant and then used for  
74 the prediction of a possible commercial scale plant.

75 Another example was carried out by Tescari et al. (2013b), who modeled a solar rotary kiln for  
76 thermochemical processes. In that work, the authors investigated different radiation models (DO,  
77 S2S) and design optimizations (insulation thickness, aperture size) of the device. CFD results were  
78 validated by comparing the temperature evolution of a specific point in the crucible wall with the  
79 temperature measured experimentally in the same point. A good agreement was found between  
80 simulation and experimental results.

81 Abanades et al. (2007b) designed and simulated a lab scale solar reactor for thermal reduction of  
82 metal oxides. In their work, a multiphase model with a Lagrangian approach was carried out to  
83 simulate the particles that were introduced continuously into a rotating cavity reactor by a screw  
84 feeder. The particles were dispersed in the cavity and dissociated in gas phase products before they  
85 could arrange a particle bed close to the crucible wall. The results of the model were used to improve  
86 the reactor during the design phase and for performance assessment.

Another work realized by Sammouda et al. (1999) was dedicated to the use of a rotary kiln as thermal particle receiver to produce industrial process heat and it included a comparison between a thermal model and experimental results. In the experiments, the kiln was continuously fed with inert sand and radiation entered the kiln through an aperture. Simulated and measured temperature profiles presented differences of about 10% near the kiln aperture, while higher differences were reported for the rest of the kiln.

Unlike the researches presented so far, this work focuses on a lab-scale rotary kiln as solar thermal receiver conceived for direct material treatment, industrial process heat, and thermal storage in solid particles above the working temperature range of molten salt (> 600 °C). The device, called University of Antofagasta Rotary Receiver (UARR), was designed and built thanks to a collaboration between the University of Antofagasta and the Renewable Energy Institute of National Autonomous University of México (IER-UNAM). The kiln, that worked in batch mode, was tested at the University of Antofagasta coupled to a 7-kW<sub>e</sub> high-flux solar simulator (HFSS) for the heating of silicon carbide (SiC) particles. A transient numerical model is developed using Matlab to predict the kiln thermal behavior and it is validated with experimental results that were also considered to assess the system. Due to the great variety of correlations existing in literature, for each heat transfer mechanism, a sensitivity analysis is carried out to select the best ones that fit with the experimental results. Finally, the model is used to assess the device under different conditions of exploitation.

## 2. Experimental set up

### 2.1. University of Antofagasta's Rotary Receiver

A solar rotary kiln is a common rotary kiln that presents an aperture at one of its ends. In this way, the solar radiation can enter inside the device and impinges directly on the moving particles. (Alonso et al., 2017a).

The UARR has a rotating cylindrical cavity or crucible of high-density alumina with a longitudinal length ( $L$ ) of 76 mm and 31 mm in inner radius ( $R$ ). To reduce reflection losses, the kiln presents a smaller aperture with a radius ( $R_{ap}$ ) of 20 mm, open to the ambient and a conical frustum with a diameter of 32 mm. The cavity is insulated with low-density alumina and it is contained in a fixed steel casing (see Fig. 1a and b). An electric motor allows the control of the cavity rotation (see Fig. 2). The kiln works in batch mode and its longitudinal axis is placed in horizontal position. It is versatile because it can be utilized with or without transparent windows and with or without carrier gases to create a controlled atmosphere. For the experiments presented hereafter, no windows were used, and no gases were introduced in the rotating chamber. For these reasons, in this work the kiln should be considered as a solar receiver rather than a solar reactor.

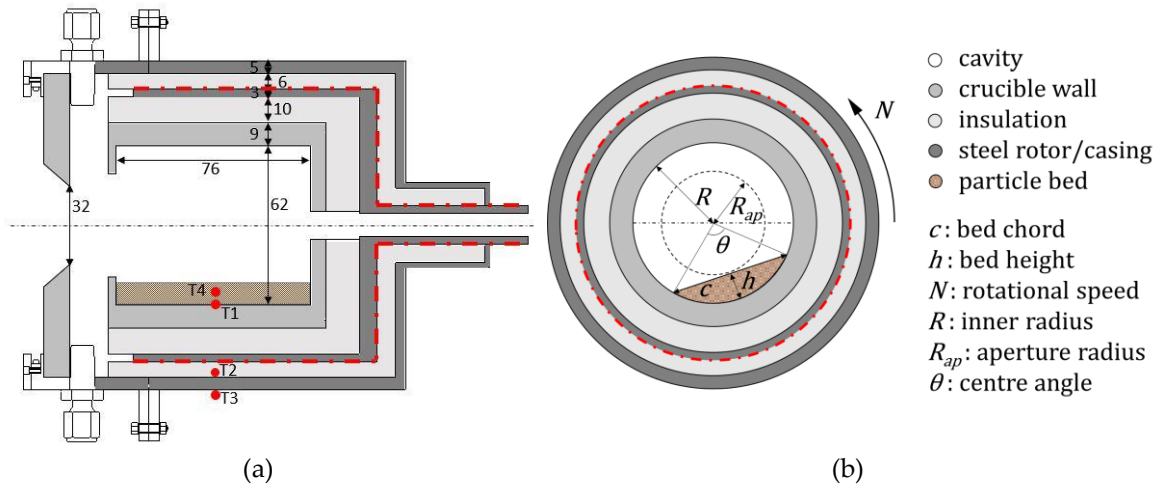
Values of Fill Ratio (or degree of fill,  $FR\%$ ) are limited in a range from 10 to 25% to achieve a good mixing of particles, corresponding to rolling and cascading bed-motion according to Mellmann classification (Mellmann, 2001). In order to avoid leakage of particles through the kiln aperture, a  $FR\%$  close to 10% was employed in the trials. To ensure the rolling bed-motion, the rotational speed ( $N$ ) was fixed to 7.5 rpm and a Froude Number ( $Fr$ ) close to  $10^{-3}$  was obtained according to equation 1,

$$Fr = \frac{\omega^2 R}{g} = \frac{(2\pi N)^2 R}{3600 g} \quad (1)$$

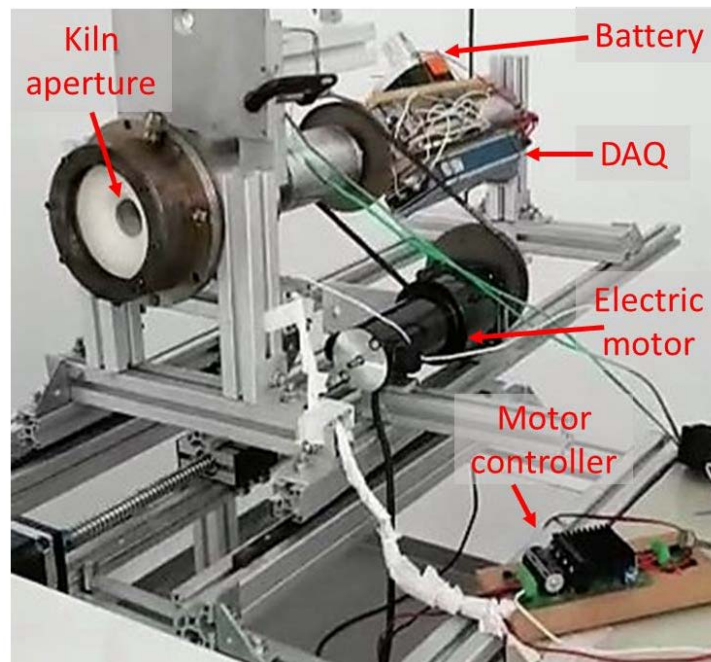
where  $\omega$  is the angular speed,  $R$  the inner radius of the crucible and  $g$  the gravity acceleration (Mellmann, 2001).

At the beginning of the campaign, a thermocouple (T1, Fig 1a) was introduced in the cavity, shielded from radiation and fixed to the inner wall. The rotating thermocouple was connected to a wireless Data Acquisition System (DAQ) that was fed by an electric battery (see Fig. 2) and both rotated together with the kiln rotor. Two more thermocouples (T2 and T3) were placed in different layers of the static UARR casing as reported in Fig. 1a and they were connected directly to a fixed DAQ. Another thermocouple (T4) was introduced inside the particle bed during the experiments.

134



135 Fig. 1. (a) Sketch of the rotary kiln longitudinal section. Lengths in millimeter. (b) Kiln transversal section. Red  
136 dash-dotted lines delimit inner rotating components from external static ones.



137

138

Fig. 2. Rotary kiln set up

## 139 2.2. Solar simulator

140 The solar simulator (Xenolux Lamphouse model of Proyecson) was installed at Solar  
141 Concentration Laboratory of Antofagasta University (LaCoSA.). The device is an adapted cinema  
142 projector analogous to those used as 7-kWe high-flux solar simulator (HFSS) by various solar research  
143 institutes of different countries (Abedini Najafabadi and Ozalp, 2018; Gallo et al., 2017; Gomez-Garcia  
144 et al., 2011). The HFSS consists mainly of a xenon short-arc lamp placed at the first focus of a truncated  
145 ellipsoidal reflector, which concentrates the lamp light on the second focus. The solar simulator  
146 shutter can open or totally close the gate aperture where the light passes through it. Despite this HFSS  
147 was used in several researches, results from characterizations realized in different institutes vary  
148 considerably. For instance, peak fluxes in a range of 1950 - 3800 kW m<sup>-2</sup> and thermal powers of 1.6 -  
149 2.1 kW can be achieved within circular areas of 110-mm radius, according to measurements reported  
150 in Bellan et al. (2013b); Gómez et al. (2011), Sarwar et al. (2014). This difference can be explained  
151 because a variation of a few millimeters in the relative reflector-lamp position can generate different

152 flux distributions on a receiver plane located at a fixed distance from the source (Gallo et al., 2017).  
 153 Then, the solar simulator of University of Antofagasta was also subjected to a characterization  
 154 procedure. Because the high intensity of the radiation flux and the power at the focal plane could  
 155 lead to steady-state temperatures higher than the desired ones (up to 850 °C), the UARR aperture  
 156 was placed in a plane with a lower peak flux. The distance  $d_0$  of the selected plane was 120 mm  
 157 longer than the focal length. In this plane, the measured irradiance peak was approximately 800  
 158 kW·m<sup>-2</sup> and the power inside a circumference of 32 mm in diameter was 360 W. An uncertainty of  
 159 ±12% for the power could be assumed for the methodology followed in the HFSS characterization  
 160 (Krueger, 2012; Sarwar et al., 2014).



161  
 162

Fig. 3. UARR located opposite to the HFSS at LaCoSA.

### 163 2.3. Experimental procedure

164 As indicated above, at the beginning of the campaign, the position of the UARR opposite to the  
 165 solar simulator was defined. Due to the conic shape of concentrated light, the UARR distance from  
 166 the solar simulator affected directly the power intercepted by the kiln. The selected distance ( $d_0$ )  
 167 should deliver a steady-state temperature in the cavity in a range of 750 - 850 °C, that are typical  
 168 values for particle receivers (Ho, 2016). Furthermore, to completely ensure that thermal shocks are  
 169 avoided in the ceramic components (frustum and crucible), at the beginning of each trial, the kiln was  
 170 located 30 mm farther (150 from the focal length) where the radiative flux had a lower concentration  
 171 level than at  $d_0$  position. When temperature in the cavity (measured by T1) overcame 100 °C, the  
 172 rotary kiln was moved through an automatic axis to  $d_0$ .

173 To properly evaluate the kiln operation, the process was divided in 4 steps (or phases):  
 174 preheating, particle loading, heating and cooling. In the first step (P1), when the solar simulator was  
 175 turned on, the empty kiln was preheated until a steady state which was defined according to the  
 176 following criterion: a temperature variation of less than 1% in a period of half an hour. In the second  
 177 phase (P2), the shutter of the solar simulator was closed, the particles were loaded inside the rotating  
 178 receiver and another thermocouple (T4) was introduced in the cavity and adjusted to maintain a  
 179 position inside the particle bed, avoiding the direct irradiation of the solar simulator (see Fig. 1a). At  
 180 that moment, the simulator shutter was opened and phase 3 (P3) started. Heating was stopped when  
 181 a steady state of the loaded reactor was reached. Radiation source was turned off and the system was

182 cooled down (P4). In an industrial application, the fourth step is not present and hot particles are  
 183 removed from the kiln and stored or directly used at high temperature. Because the last phase is not  
 184 the aim of the system analysis for the proposed applications, temperature measurements were  
 185 stopped before the system returned completely to room temperature. The whole process was realized  
 186 three times to ensure its repeatability.

187 Table 1. Process parameters in each step.

| Steps           | Rotational speed (rpm) | Particle mass (g) | HFSS state | Model start time (minute) |
|-----------------|------------------------|-------------------|------------|---------------------------|
| P1 - Preheating | 0                      | 0                 | On         | 0                         |
| P2 - Loading    | 7.5                    | 0-43              | Off        | 165                       |
| P3 - Heating    | 7.5                    | 43                | On         | 169                       |
| P4 - Cooling    | 7.5                    | 43                | Off        | 252                       |

188

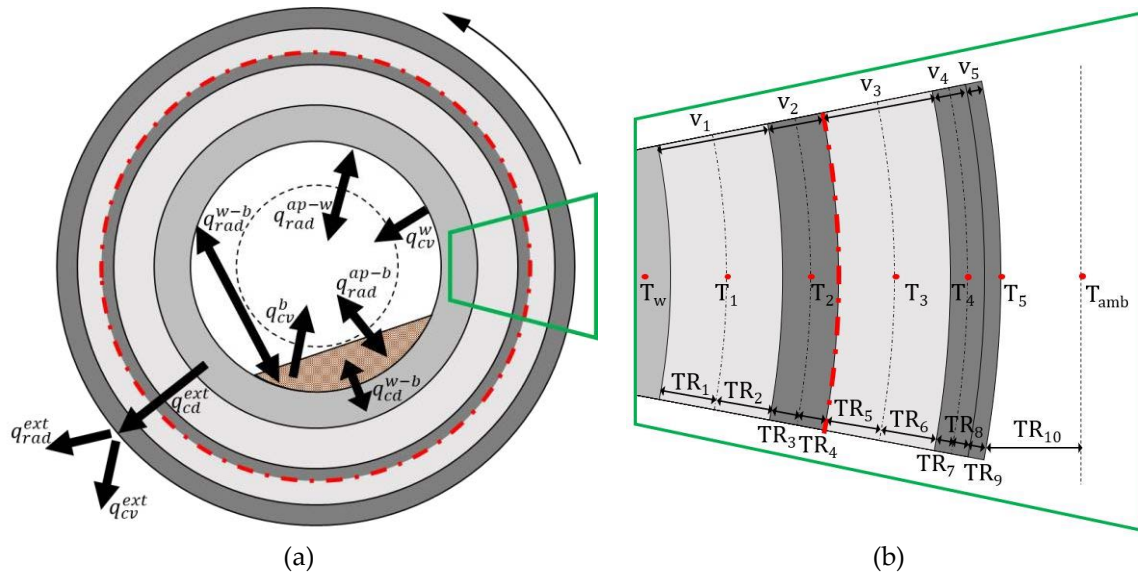
### 189 3. Rotary kiln thermal model

190 To determine the temperatures of the granular bed and the kiln wall, it is required to assess the  
 191 heat transfer mechanisms involved in the process. In the case of the UARR, as well as in the most  
 192 solar receivers, the mechanisms of conduction, convection and radiation are present. According to  
 193 Incropera et al. (2011b), due to the complexity of the system, an analytical solution of the temperature  
 194 during the process is not possible to find. Therefore, a numerical transient one-dimensional thermal  
 195 model is developed using a Matlab code and it is validated with experimental results of the test  
 196 campaign performed at LaCoSA. In the numerical model, the process time is discretized considering  
 197 a constant time step ( $\Delta t$ ) for all the phases. The maximum time step size is limited by a numerical  
 198 criterion indicated in Appendix C. The model is based on energy balances defined for the particle  
 199 bed, the crucible wall, and the kiln shell at each time step. In Fig. 4a, a schematic representation of  
 200 the heat fluxes evaluated in the model is reported. A double-direction arrow is shown when the heat  
 201 flux direction can change. Convection heat transfers are considered with the environment at room  
 202 temperature between both particles and wall surface. Single-direction arrows are used. As can be  
 203 deduced from that figure, energy balances defined for the granular bed and the crucible wall are  
 204 interconnected by the radiative and conductive power exchanged between them. At the same time,  
 205 the temperature in the crucible is influenced by the power transferred from the wall to the rest of the  
 206 kiln shell. Additionally, Fig. 4b shows the control volumes and the calculation elements, in which is  
 207 discretized the kiln, to estimate the radial temperature along the shell.

208 Several simplifications are considered in the model in order to reach short computation times  
 209 (less than three minutes in a computer with i7-8700 processor 3.2GHz and 16 GB RAM) but, at the  
 210 same time, to achieve enough precision for the evaluation of the kiln thermal behavior. The  
 211 approximations assumed in the model are indicated hereunder.

- 212 • Lumped capacitance analyses are carried out for the crucible wall and the particle bed. To do  
 213 that Biot numbers ( $Bi$ ) are assessed.  $Bi$  represents the ratio between heat transfer by convection  
 214 and by conduction for a specific body. When the  $Bi$  is lower than 0.1, it is possible to develop a  
 215 lumped capacitance analysis with an associated error lower than 5% in the temperature  
 216 distribution inside the body. As general rule, the smaller the  $Bi$  the smaller the error (Cengel,  
 217 2002; Incropera et al., 2011b). With these analyses, conduction is considered the main mechanism  
 218 for the heat transfer. Therefore, uniform temperatures can be considered at each time step for  
 219 the crucible wall, and the granular material.
- 220 • Another approximation is related to the radiation exchange between surfaces. When several  
 221 surfaces are involved, the view factors cannot be evaluated by simple analytical expressions  
 222 Hence, to simplify this assessment, the interior UARR-cavity envelope ( $A_{cav}$ ) is divided in three  
 223 surfaces: aperture ( $A_{ap}$ ), particle bed ( $A_b$ ) and inner crucible wall ( $A_w$ ) as shown in Fig. 5a.

- 224 • It is also considered that  $A_{ap}$  is a flat surface with a constant room temperature and with an  
 225 emissivity/absorptivity equal to one.  
 226 • Furthermore, to estimate the temperature inside the different material layers which contain and  
 227 insulate the cavity, UARR is considered as a finite cylinder with adiabatic bases. It means that  
 228 losses are only considered from lateral walls. This is justified because the thicknesses of  
 229 insulating materials and air layers at UARR bottom and front parts are considerably higher than  
 230 the ones of lateral wall.  
 231 • Particle bed cross section ( $A_b^{tr}$ ) is approximated by a circular segment. From this assumption, the  
 232 main geometrical parameters relative to the granular bed can be calculated (see Appendix A).  
 233 • Longitudinal gradients are considered as an average value of different kiln transversal sections.  
 234 Nevertheless, in receivers larger than the UARR, radial and axial temperature gradients could  
 235 be not negligible, and a three-dimensional analysis is recommended to reduce estimation errors.  
 236 • According to manufacturer data sheet (Industrial Comercial Chile Ltda., 2018), particles are  
 237 composed of a mix of different materials (SiC, C, Fe, Al, SiO<sub>2</sub>) where 96.5% is SiC. Therefore,  
 238 each particle property corresponds to the weighted average of the material properties that  
 239 compose the blend. Conductivities and specific heat capacities present remarkable changes in  
 240 the operation temperature range (0-800 °C). Hence, in the model, their values are varied with  
 241 the corresponding material temperature (see tables in Appendix B). Nevertheless, material  
 242 emissivity, absorptivity and reflectivity also change with temperature, direction and  
 243 wavelength, but no many studies have been realized at high temperatures (100 -1000 °C) in  
 244 the range of visible and near infrared. Therefore, in this case, as in most practical situations, an  
 245 average constant emissivity for all directions, wavelengths (gray surface assumption), and  
 246 temperature is used (Valencia and Queded, 2008).  
 247



248 Fig. 4. (a) Heat fluxes in the cross section of the kiln. Red dash-dotted circumference separates inner rotating  
 249 elements from external static ones. (b) Magnification of the green area which shows the control volumes and the  
 250 thermal resistances of each element used in the numerical model (image scale is not respected). Material colors  
 251 are the same as in previous figures of the kiln.  
 252

256 As mentioned in the description of the experimental process, the kiln works under different  
 257 conditions and the model is able to simulate the kiln behavior when the boundary conditions change,  
 258 as indicated in table 1. For instance, when the crucible is empty, the heat fluxes related with the  
 259 granular bed are not present. In this situation, the radiative exchanges from the bed with the aperture  
 260 ( $q_{rad}^{ap-b}$ ) or the wall ( $q_{rad}^{w-b}$ ), convection losses ( $q_{cv}^b$ ), and the conductive heat transfer between the  
 261 particles and the wall ( $q_{cd}^{w-b}$ ) are not considered in the model. When the SiC is inside the cavity, all  
 262 the heat fluxes depicted in Fig. 4a and the associated thermal losses are calculated at each time step.

263 The powers associated to the radiative fluxes exchanged between two surfaces ( $Q_{rad}^{x-y}$ ) are  
 264 calculated considering equation 2,

$$Q_{rad}^{x-y} = -Q_{rad}^{y-x} = A_x F_{x-y} (J_x - J_y) = A_y F_{y-x} (J_y - J_x) \quad (2)$$

265 where  $A_x$  is the area of a generic surface  $x$ ,  $F_{x-y}$  is the view factor of the surface  $y$  from the  
 266 surface  $x$ , and  $J_x$ ,  $J_y$  are the radiosities of surface  $x$  and  $y$ . The radiosity  $J_x$  is defined as the sum of  
 267 the emitted and reflected radiative flux by the  $x$ -surface.

275 To calculate convective losses, the methodology developed in a previous work of the authors is  
 276 applied (Gallo et al., 2018). In an open cavity rotary kiln, inner convective losses ( $Q_{cv}^l$ ) are expected to  
 277 be like those generated in a static solar cavity receiver. Several correlations have been proposed and  
 278 used by many authors to calculate them (Li et al., 2010; Ma, 1993; McDonald, 1995; Siebers and  
 279 Kraabel, 1984). In this work, the methodology proposed by Siebers and Kraabel (Siebers and Kraabel,  
 280 1984) is followed. Convection losses are split in forced ( $fc$ ) and natural ( $nc$ ) contributions for both bed  
 281 and wall surfaces (see Appendix B2). However, a rotary kiln is not exactly the same as a still receiver;  
 282 hence, to take into account the kiln rotation and the effects on the particle bed, a correction factor ( $f_{cv}^b$ )  
 283 is used. According to Tscheng and Watkinson (1979), convections on particles could be up to one  
 284 order of magnitude higher than kiln walls. Sammouda et al. (1999) reported that the convective  
 285 coefficient for particles was about five or six times the value of the coefficient for the cavity wall. This  
 286 is due mainly to the underestimation of considering the plane chord area as the surface of the  
 287 convective heat exchange. For this reason, the expressions of the convective losses from the wall and  
 288 the granular bed are differentiated.

$$Q_{cv}^l = Q_{cv}^w + Q_{cv}^b \quad (3)$$

$$Q_{cv}^w = h_{cv} \cdot (T_w - T_{amb}) \cdot A_w \quad (4)$$

$$Q_{cv}^b = h_{cv} \cdot (T_b - T_{amb}) \cdot A_b \cdot f_{cv}^b \quad (5)$$

291 Once  $h_{cv}$  is known, in order to check the validity of the lumped capacitance analysis approach,  
 292 Biot numbers for wall and bed are calculated. Both should be lower than 0.1.

$$Bi_w = Lc_w \cdot \frac{h_{cv}^w}{K_w} \text{ with } Lc_w = L \quad (6)$$

$$Bi_b = Lc_b \cdot \frac{h_{cv}^b}{K_b} \text{ with } Lc_b = V_b / (A_b \cdot f_{cv}^b) \quad (7)$$

294 The heat transfer between the covered wall and the bulk bed is also included in the model. To  
 295 do that, an exchange coefficient ( $h_{w-b}$ ) is used. Several correlations have been proposed to assess the  
 296 contact heat transfer between the inner kiln wall and the granular material. However, the values of  
 297 this coefficient predicted by the different correlations are not in agreement. Herz et al. (2012)  
 298 compared four of the most used models (Li et al., 2005; Schlunder and Mollekopf, 1984; Tscheng and  
 299 Watkinson, 1979; Wes et al., 1976) with the experimental results achieved in a indirectly heated lab-  
 300 scale rotary drum. Materials, particle size, filling degree and rotational speed were varied for a  
 301 sensitivity analysis. They found that the correlation by Li et al. had a reasonable agreement with the  
 302 experimental results.

303 However, in most of the models,  $h_{w-b}$  is related to the effective conductivity of the bulk  
 304 material ( $K_b$ ). Even for  $K_b$ , numerous correlations are available in literature. Abyzov et al. (2013)  
 305 resumed most of them and indicated that the real value of  $K_b$  for a granular material should be  
 306 included between the lowest value, obtained by Maxwell model (Maxwell, 1873), and the highest one  
 307 evaluated by the effective medium theory (EMT) analyzed in Carson et al. (2005). Because of the great  
 308 variety of models and theories with discordant results, a sensitivity analysis of these parameters is  
 309 carried out in order to find the best values that fit to the experimental data. To assess the results, the  
 310 root-mean-square error (RMSE) and the mean absolute percentage error (MAPE) are calculated for  
 311 wall and particle temperatures (mathematical expressions are included in Appendix D).

312 Losses from the external casing ( $Q_l^{ext}$ ) can be calculated using equation 8,

$$Q_i^{ext} = Q_{cd}^{ext} + Q_{rad}^{ext} + Q_{cv}^{ext} = \sum_{i=1}^5 m_i c p_i \cdot \frac{T_i^t - T_i^{t-1}}{\Delta t} + \frac{T_5^t - T_{amb}}{TR_{10}} \quad (8)$$

313 where  $m_i$ ,  $cp_i$ ,  $T_i^t$ , and  $T_i^{t-1}$  are the mass, the specific heat, and the temperatures of the i-  
 314 control volume at the t-instant and (t-1)-instant,  $T_5^t$  is the external temperature of the kiln casing,  
 315  $T_{amb}$  is the room temperature,  $TR_{10}$  is the thermal resistance for convection and radiation of the  
 316 tenth element, and  $\Delta t$  is the time step. These losses include the energy stored due to the thermal  
 317 capacity of the insulation, rotor and casing.

318 Once all the heat fluxes and the relative thermal powers are known, the energy balances are  
 319 defined and the new temperatures of particle bed and at the t-instant are calculated from equations  
 320 9 and 10.

$$Q_{net}^b = \frac{m_b c p_b (T_b^t - T_b^{t-1})}{\Delta t} = Q_{rad}^{ap-b} + Q_{rad}^{w-b} + Q_{cd}^{w-b} - Q_{cv}^b \quad (9)$$

$$Q_{net}^w = \frac{m_w c p_w (T_w^t - T_w^{t-1})}{\Delta t} = Q_{rad}^{ap-w} - Q_{rad}^{w-b} - Q_{cd}^{w-b} - Q_{cv}^w - Q_l^{ext} \quad (10)$$

334 Considering that the performed experimental tests included phases where the solar simulator is  
 335 turned on and off,  $Q_{in}$  is defined by equation 11.

$$Q_{in}^t = \begin{cases} 369 \text{ W} & \text{if } t < t_{PH} \text{ or } t_L < t < t_H \\ 0 & \text{if } t_{PH} < t < t_L \text{ or } t_H < t < t_{end} \end{cases} \quad (11)$$

336 where  $t$  is a generic instant from  $t_0$  to  $t_{end}$  (last instant of simulation),  $t_{PH}$  is the instant when the  
 337 heating of the empty UARR stops and the solar simulator is turned off, before the particle loading  
 338 (end of the preheating phase).  $t_L$  is the moment when particles are already inserted in the UARR and  
 339 the solar simulator is turned on (end of the particle loading phase and start of the heating phase).  $t_H$   
 340 is the moment when the solar simulator is turned off and particle heating stops (end of the heating  
 341 phase). After  $t_H$ , cooling phase starts.

342 Particles were introduced into the UARR at a certain instant  $t_p$  between  $t_{PH}$  and  $t_L$ , and  
 343 loading operation lasted up to thirty seconds. For sake of simplicity, in the model, particle-bed mass  
 344 changes instantaneously from zero to the value corresponding to the particle-bed mass  
 345 approximately thirty second before the end of loading phase.

346 A detailed description of the thermal model is reported in the Appendix C.

### 347 3.1. UARR efficiency

349 At each time step, kiln efficiency ( $\eta_{UARR}^t$ ) can be calculated as the ratio between the energy absorbed  
 350 by the particles ( $En_{net}^b$ ) and the thermal energy entering the cavity that is supplied by the solar  
 351 simulator ( $En_{in}$ , see equation 12). Spillage losses are not considered, because the solar simulator is  
 352 not optimized for this system and the flux distribution is larger than kiln aperture.

$$\eta_{UARR}^t = \frac{En_{net}^b}{En_{in}} = \frac{m_b \cdot \sum_{t_0}^t c_p^t \cdot (T_b^t - T_b^{t-1})}{\sum_{t_0}^t Q_{in}^t \cdot \Delta t} \quad (12)$$

353 In this case,  $t$  is a generic instant between  $t_0$  (simulation starting point) and  $t_{end}$ .

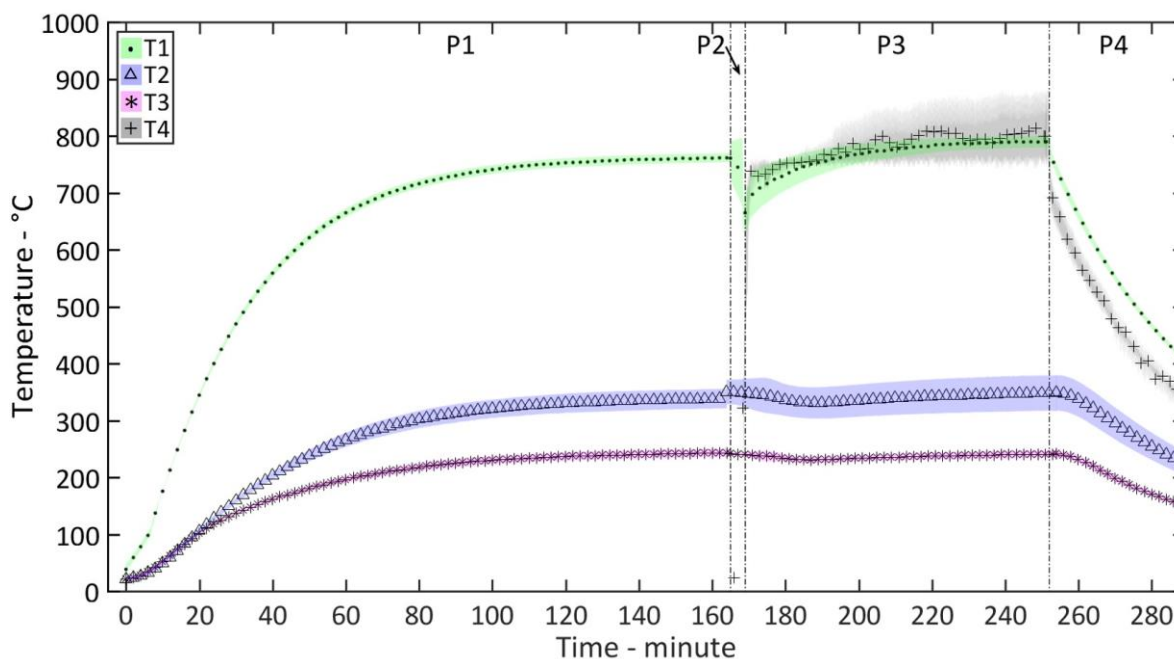
## 354 4. Results and discussion

### 355 4.1. Experimental tests

356 Experimental data were obtained thanks to the experimental tests conducted at LaCoSA of  
 357 University of Antofagasta. As mentioned before, the process was divided in 4 phases. During P1, the  
 358 kiln was maintained without rotation irradiated by the HFSS; when temperature in the cavity (T1)  
 359 overcame 100 °C, the rotary kiln was moved through an automatic axis to  $d_0$ . The UARR was heated  
 360 until it reached the steady state; then the simulator shutter was closed and P2 started. At this point,

361 a constant rotation speed of 7.5 rpm was applied to the kiln. The system operated under these  
 362 conditions during approximately three minutes until to reach a new steady state and then, 0.043 kg  
 363 (corresponding to a FR = 10%) of particles were loaded into the UARR. Loading operation lasted  
 364 almost thirty seconds. Afterwards, another thermocouple (T4) was introduced in the cavity and it  
 365 was positioned inside the core of the particle bed. Just then, the simulator shutter was opened (P3).  
 366 The heating phase was stopped when the last steady state was reached, and the radiation source was  
 367 turned off. At that time, P4 begun and the system was cooled down. Temperature measurements  
 368 reported in Fig. 5 correspond to the average values with their uncertainty band. Upper and lower  
 369 band limits are the sum and the difference of the average value with uncertainties calculated at each  
 370 sampling instant (see Appendix D for a mathematical description). Note that temperature values  
 371 delivered by T4 present a wider error band, due to the difficulty to maintain the thermocouple in a  
 372 fixed position in the core of the bed. However, registered values present a coherent behavior, as well  
 373 as their comparison with the simulated results described in section 4.2. Another thermocouple (not  
 374 indicated in the figures) measured room temperature that changed from 20 °C at the beginning of the  
 375 trial to a maximum of 26 °C at the end of P3. In Fig. 5, at the end of P1, thermocouple T1 reaches  
 376 approximately 760 °C. During P2, temperature of T1 decreases 20 °C after the shutter closing, and an  
 377 additional decrement until 660 °C was registered when SiC particles were introduced in the cavity.  
 378 Meanwhile, an increment from ambient temperature to 500 °C is measured by T4 in the last forty  
 379 seconds of P2 (see Fig. 7). One minute after the solar simulator was turned on, the temperature of T4  
 380 exceeded the crucible temperature measured by T1. At the end of P3, a maximum wall temperature  
 381 of 790 °C was achieved in the middle of the crucible (T1), and the thermocouple inserted in the  
 382 particle bed (T4) was measuring in a range of 800 – 820 °C. This gap is due to the kiln rotation which  
 383 affected radial and longitudinal position of T4 inside the particle bed.

384 From these experimental results, it could be inferred that SiC heating is very quick compared to  
 385 UARR heating, because mass introduced into the kiln was approximately one hundred times less  
 386 than UARR mass. Moreover, the range of temperature accomplishes the objective of the campaign  
 387 and demonstrates the feasibility to heat up particles in a solar rotary kiln for thermal storage as well  
 388 as for industrial process heat applications above the working temperature range of molten salt.  
 389



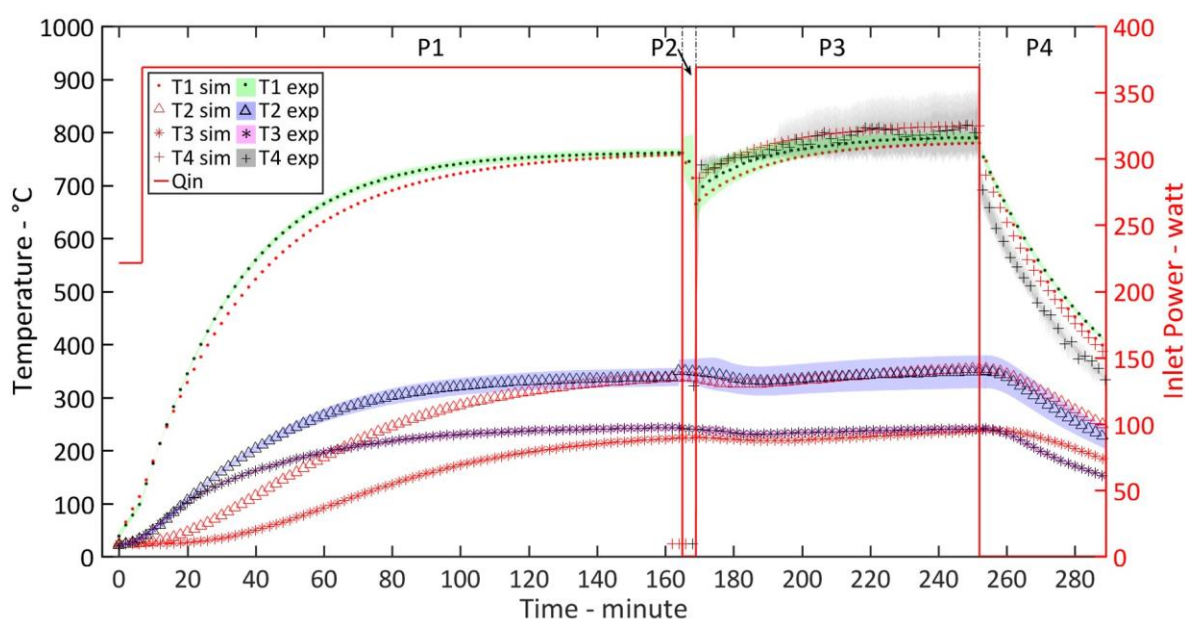
390 Fig. 5. UARR experimental temperature profiles with corresponding error band.  
 391  
 392  
 393  
 394

## 395 4.2. Model validation

396 To define which model should be used for the estimation of  $f_c$ ,  $K_b$ , and  $h_{w-b}$ , a sensitivity  
 397 analysis is carried out. Each of the four correlations (Wes, Tscheng, Li, and Schlunder) of  $h_{w-b}$   
 398 compared in Herz, is combined with the Maxwell (M) and the EMT model of  $K_b$ , for each selected  $f_c$   
 399 ( $f_c = 1, 3, 3.5, 4, 5$ ). As can be seen from table 2, the Biot numbers of both, wall and bed result always  
 400 less than 0.1, except for some cases when  $f_c = 1$ . In fact, the kiln rotation improves the thermal  
 401 homogenization of the particle bed and helps to balance the spatial temperature differences.

402 Best fits are obtained when the RMSE and MAPE are minimized. Cases with Wes or Tscheng  
 403 models combined with the EMT model are not shown in the table 2, because the achieved  $h_{w-b}$  are  
 404 too high and lead to results without physical explanation. Reasonable values are obtained when  $f_c =$   
 405 3.5 for Wes-M and Li-EMT combinations. In particular, MAPE reached a minimum value of 5.1% for  
 406 the Li-EMT and RMSE are in most of the cases lower than 20 °C. Highest values of RMSE are achieved  
 407 for the particle temperature during P2. This is due to the fast increment of the particle bed  
 408 temperature, approximately 20 K s<sup>-1</sup>. However, this behavior is present only during the last forty  
 409 seconds of P2.

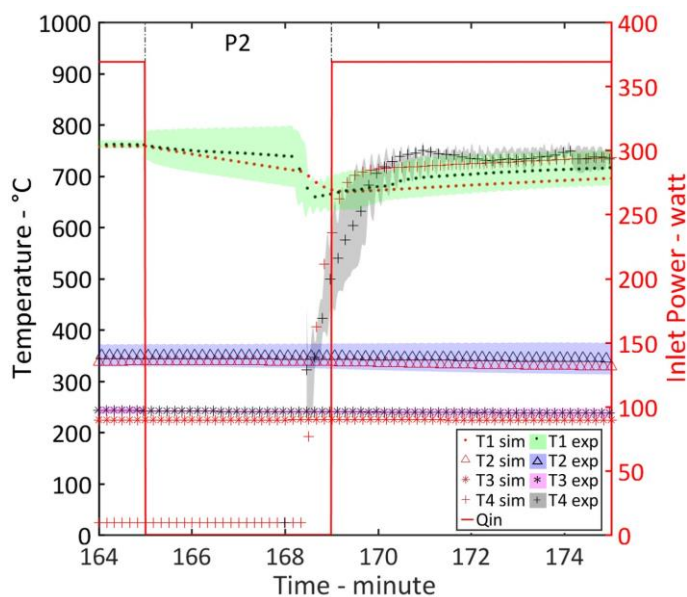
410 In the final evaluation of this work, results obtained with the Li-EMT with a  $f_c = 3.5$  are used to  
 411 assess the kiln performances. Figures 6 and 7 show the comparison between simulated temperature  
 412 profiles and the experimental data. The same four phases of the thermal process are reproduced in  
 413 the model with the conditions summarized in table 1. The axial movement of the kiln could be  
 414 appreciated in Fig. 6, where after the first seven minutes the inlet power changes from a value of  
 415 almost 222 W to 369 W. A one-second time step is used in the model. This time step agrees with the  
 416 limitations indicated above and corresponds to the experimental frequency of measurements.  
 417 However, for a better description of the data obtained, in Fig. 5 and 6 the results are indicated with a  
 418 time interval of two minutes and, in Fig. 7, every ten seconds.  
 419



420 Fig. 6. Thermal behavior of UARR when irradiated with the solar simulator. Comparison of experimental  
 421 (exp) and simulated (sim) temperature profiles. Experimental data are provided with respective colored  
 422 uncertainty band. Right y-axis shows the inlet power ( $Q_{in}$ ) used in the model.  
 423  
 424

425 Table 2. Sensitivity analysis results.

|    | $f_{cv}$ | $h_{w-b}$<br>model | $K_b$<br>model | $h_{w-b}$ | $K_b$ | Biot<br>bed | Biot<br>wall | RMSE<br>bed P2 | RMSE<br>bed P3 | RMSE<br>bed P4 | RMSE<br>wall P2 | RMSE<br>wall P3 | RMSE<br>wall P4 | MAPE<br>total |
|----|----------|--------------------|----------------|-----------|-------|-------------|--------------|----------------|----------------|----------------|-----------------|-----------------|-----------------|---------------|
| 1  | 1        | Wes                | M              | 645       | 0.33  | 0.2056      | 0.0091       | 50             | 88             | 137            | 17              | 50              | 75              | 7.60          |
| 2  | 1        | Tscheng            | M              | 1575      | 0.33  | 0.2083      | 0.0091       | 197            | 68             | 147            | 15              | 58              | 79              | 7.68          |
| 3  | 1        | Li                 | M              | 386       | 0.34  | 0.2031      | 0.0090       | 108            | 108            | 128            | 18              | 43              | 71              | 7.53          |
| 4  | 1        | Li                 | EMT            | 794       | 20.30 | 0.0034      | 0.0091       | 72             | 81             | 140            | 16              | 52              | 76              | 7.62          |
| 5  | 1        | Schlunder          | N.a.           | 3840      | N.a.  | 0.0033      | 0.0092       | 273            | 59             | 151            | 14              | 61              | 81              | 7.72          |
| 6  | 3        | Wes                | M              | 627       | 0.32  | 0.0688      | 0.0084       | 46             | 28             | 61             | 17              | 8               | 8               | 5.29          |
| 7  | 3        | Tscheng            | M              | 1524      | 0.32  | 0.0696      | 0.0084       | 192            | 17             | 73             | 15              | 9               | 11              | 5.34          |
| 8  | 3        | Li                 | M              | 373       | 0.32  | 0.0681      | 0.0083       | 111            | 44             | 48             | 18              | 12              | 6               | 5.36          |
| 9  | 3        | Li                 | EMT            | 770       | 22.52 | 0.0010      | 0.0084       | 67             | 24             | 64             | 16              | 8               | 9               | 5.29          |
| 10 | 3        | Schlunder          | N.a.           | 3735      | N.a.  | 0.0010      | 0.0085       | 270            | 16             | 79             | 14              | 10              | 13              | 5.42          |
| 11 | 3.5      | Wes                | M              | 623       | 0.32  | 0.0591      | 0.0082       | 45             | 16             | 44             | 17              | 16              | 11              | 5.12          |
| 12 | 3.5      | Tscheng            | M              | 1513      | 0.31  | 0.0597      | 0.0083       | 191            | 15             | 57             | 15              | 10              | 11              | 5.14          |
| 13 | 3.5      | Li                 | M              | 370       | 0.32  | 0.0584      | 0.0082       | 112            | 29             | 30             | 18              | 23              | 12              | 5.25          |
| 14 | 3.5      | Li                 | EMT            | 764       | 22.99 | 0.0008      | 0.0082       | 66             | 13             | 47             | 16              | 14              | 11              | 5.10          |
| 15 | 3.5      | Schlunder          | N.a.           | 3710      | N.a.  | 0.0008      | 0.0083       | 270            | 19             | 63             | 14              | 8               | 11              | 5.20          |
| 16 | 4        | Wes                | M              | 619       | 0.31  | 0.0517      | 0.0081       | 44             | 11             | 28             | 17              | 27              | 25              | 5.17          |
| 17 | 4        | Tscheng            | M              | 1501      | 0.31  | 0.0523      | 0.0081       | 190            | 22             | 42             | 15              | 21              | 24              | 5.23          |
| 18 | 4        | Li                 | M              | 367       | 0.32  | 0.0512      | 0.0080       | 113            | 17             | 15             | 18              | 34              | 26              | 5.26          |
| 19 | 4        | Li                 | EMT            | 758       | 23.44 | 0.0007      | 0.0081       | 64             | 13             | 32             | 16              | 25              | 24              | 5.17          |
| 20 | 4        | Schlunder          | N.a.           | 3686      | N.a.  | 0.0007      | 0.0082       | 269            | 28             | 48             | 14              | 18              | 23              | 5.29          |
| 21 | 5        | Wes                | M              | 611       | 0.31  | 0.0415      | 0.0078       | 42             | 30             | 10             | 17              | 49              | 52              | 5.67          |
| 22 | 5        | Tscheng            | M              | 1478      | 0.31  | 0.0419      | 0.0079       | 188            | 43             | 16             | 15              | 43              | 52              | 5.70          |
| 23 | 5        | Li                 | M              | 361       | 0.31  | 0.0411      | 0.0077       | 115            | 19             | 22             | 18              | 55              | 53              | 5.75          |
| 24 | 5        | Li                 | EMT            | 746       | 24.29 | 0.0005      | 0.0078       | 62             | 34             | 10             | 16              | 47              | 52              | 5.67          |
| 25 | 5        | Schlunder          | N.a.           | 3640      | N.a.  | 0.0005      | 0.0079       | 268            | 49             | 22             | 14              | 40              | 51              | 5.74          |



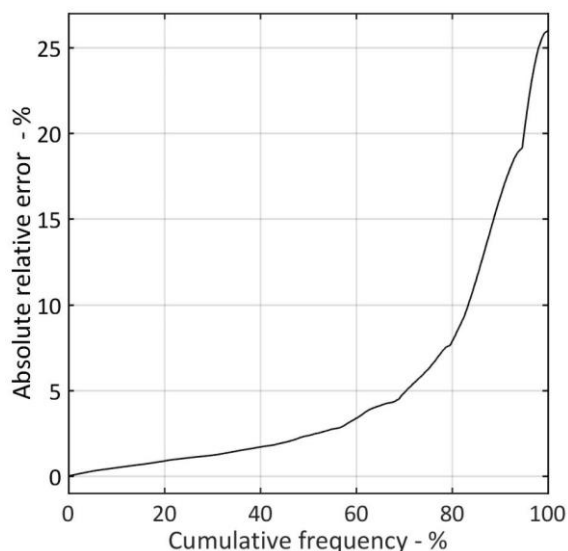
427 Fig. 7. Thermal behavior of UARR when irradiated with the solar simulator (magnification of P2 phase).  
 428 Comparison of experimental (exp) and simulated (sim) temperature profiles. Experimental data are provided  
 429 with respective colored uncertainty band. Right y-axis shows the inlet power ( $Q_{in}$ ) used in the model.  
 430  
 431

432 To evaluate the model accuracy, the absolute value of the relative error between experimental  
 433 and simulated temperatures in kelvin is calculated at each instant. Then, the relative errors obtained  
 434 from all the temperature curves are arranged in ascending order. In this way, the cumulative  
 435 frequency of the relative error can be assessed as shown in Fig. 8. Note that the percentage of the  
 436 cumulative frequency is indicated in the x-axis. From that figure it can be deduced that most of the  
 437 data present an error lower than 2.4%, and almost three quarters of the relative errors are below 6%.  
 438 In table , the MAPE is indicated for each process step and for each temperature curve. High  
 439 discrepancies relative to T2 and T3 are evident in the preheating phase. Maximum errors, up to 26%  
 440 are obtained for T3 during P1. This fact is probably due to the UARR geometry simplification and  
 441 some discrepancies may be also due to a no uniform distribution of the solar spot inside the cavity.  
 442 Furthermore, radiation spillage could contribute to heat the receiver externally and it is not included  
 443 in the model. In general, and according to the evaluation of the relative error, results coming from  
 444 the theoretical model are in good agreement with the experimental data considered.

445 Table . Percentage of the average relative error between simulated and experimental temperatures for  
 446 each process phase.

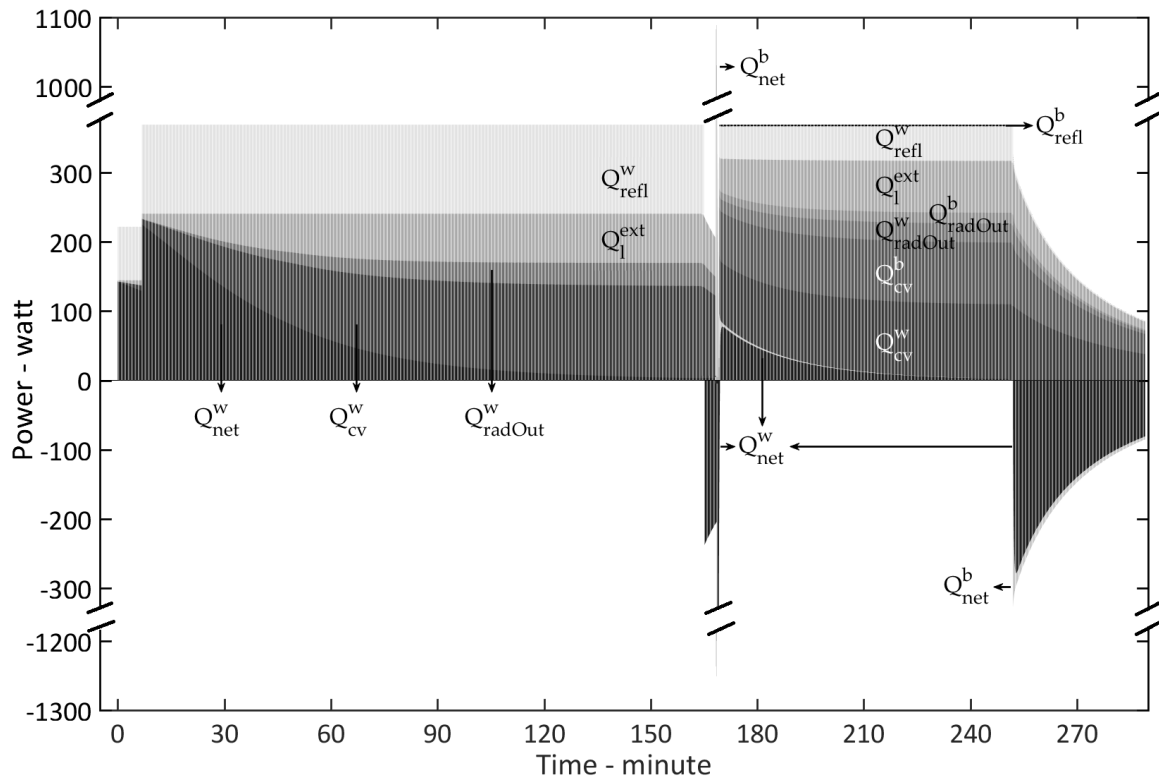
|    | P1   | P2  | P3  | P4  |
|----|------|-----|-----|-----|
| T1 | 2.2  | 1.4 | 1.3 | 1.3 |
| T2 | 8.5  | 1.9 | 0.8 | 2.9 |
| T3 | 13.7 | 3.3 | 2.1 | 4.8 |
| T4 | N.a. | 8.7 | 0.9 | 6.2 |

447  
 448



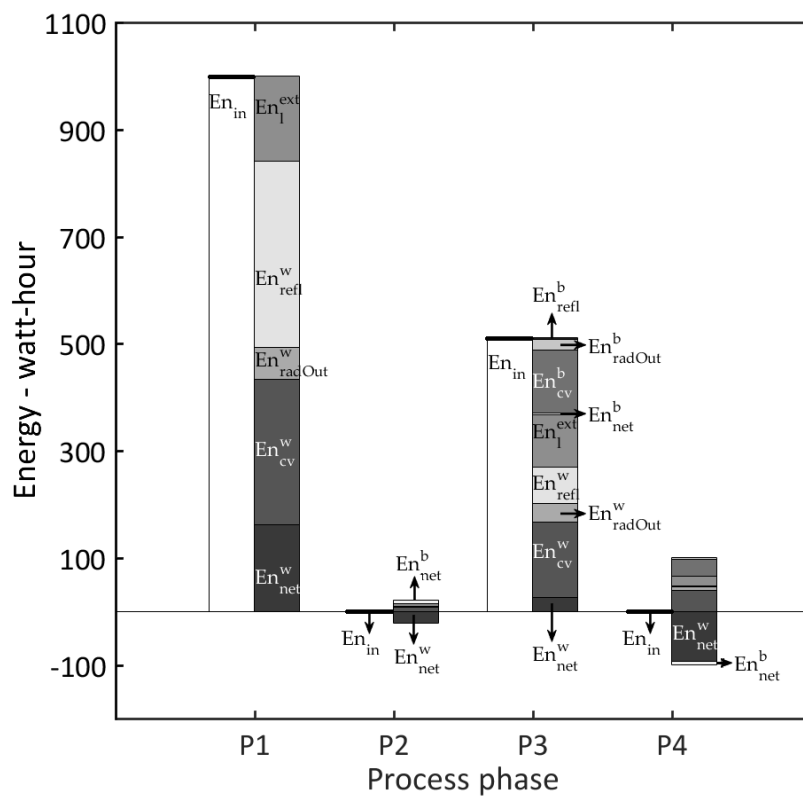
449 Fig. 8. Cumulative frequency percentage of the absolute relative error for all the temperature curves  
 450 simulated in the model and compared with experimental data.  
 451  
 452

453 This model allows the estimation of the energy gains and losses in the crucible wall during the  
 454 process. In Fig. 9,  $Q_{in}$  is represented by the sum of each contribution in which is subdivided at each  
 455 time step. At the beginning of the preheating phase, approximately 60% of the entering energy is  
 456 absorbed by the crucible wall, and 35% is reflected from the cavity to the environment. The absorbed  
 457 energy increments the crucible temperature; however, part of this energy is lost for inner cavity  
 458 convection, re-radiation and external losses from the kiln case. During loading step, when SiC  
 459 particles are introduced in the kiln,  $Q_{in}$  is zero and heat is transferred from the kiln wall to the  
 460 particles. Wall temperature decreases and  $Q_{net}^w$  is negative. Part of this energy is absorbed by the  
 461 particles ( $Q_{net}^b$  is positive). As consequence, convection, re-radiation and reflection losses from SiC  
 462 appear. Note that energy absorbed by the particles in P2 represents the 69% (6.9 Wh) of the total  
 463 energy absorbed during both P2 and P3 steps (9.9 Wh). This is reflected in the peak of Fig. 9 where  
 464 the energy stored in the wall is transferred to the SiC through radiation ( $Q_{rad}^{w-b}$ ) and conduction  
 465 mechanisms ( $Q_{cd}^{w-b}$ ). Finally, during the cooling phase,  $Q_{in}$  is zero again and the energy from the bed  
 466 and the kiln is released to the environment ( $Q_{net}^w, Q_{net}^b$  are negative). These quantities equal the sum  
 467 of the losses due to conduction, convection and radiation. As well as during P2 step, reflection losses  
 468 are almost zero because the solar simulator is off, and they are composed only by the thermal  
 469 radiation emitted and reflected by inner cavity wall and particle bed.  
 470



471  
472  
473  
474

Fig. 9. Instantaneous energy balance of UARR when tested at LaCoSA. Sum of each contribution corresponds to power entering into the UARR at each moment.



475  
476  
477  
478  
479  
480  
481

Fig. 10. Energy balance of UARR for each process phase.

Figure 10 shows the energy balance per process phase. The same contributions of Fig. 9 are now compared in terms of energy. In the left columns, there is the inlet energy ( $En_{in}$ ) and in the right columns there are the energy losses and energies stored by the cavity wall ( $En_{net}^w$ ) and the particles ( $En_{net}^b$ ). These quantities are positive if the temperature of the wall or the particles increases, and

482 negative if the temperature decreases. The sum of right column components is equal to  $En_{in}$ . Energy  
 483 stored in the rest of UARR components (insulations, steel rotor and casing) is included in the external  
 484 losses ( $En_i^{ext}$ ). It should be noted that P1 is the longest step in time and therefore, energy quantities  
 485 are greater than other phases. (the value of  $En_{in}$  in P1 is 998 Wh and in P3 is 510 Wh). In the first  
 486 step, the energy is used to heat up the UARR and compensates the thermal losses for convection  
 487 radiation and conduction. The 35% of entering energy is instantaneously reflected outside the cavity.  
 488 This is mainly related to the wall reflectivity (0.93 for ceramic alumina), and to the cavity shape which  
 489 presents a relatively large aperture to favor the incoming radiation from the HFSS. Nevertheless,  
 490 considering Lambertian surfaces and comparing the irradiance distribution on the bed and cavity  
 491 wall, the low absorptivity of the alumina lead to a more homogeneous irradiance due to a greater  
 492 amount of inner reflections, than other materials with higher absorptivity (Gallo et al., 2018). As  
 493 consequence, a uniform irradiance in the cavity should favor a uniform distribution of temperature  
 494 in the particle bed.

495 In P1, losses for convection and conduction in the empty kiln are respectively the 27% and 16%  
 496 of  $En_{in}$ , while  $En_{net}^w$  is the 16%. When the solar simulator is turned off ( $En_{in}$  is zero in P2 and P4),  
 497 the released energy to the environment come from the energy stored in the kiln wall (in P2 phase)  
 498 and from both the kiln and the particle bed (in P4 phase). In P3 the sum of convective losses from  
 499 wall and particles arise to 51% of entering energy and losses for conduction are 19% of  $En_{in}$ . The  
 500 reflected losses decrease notably in comparison to those calculated for the first step: radiation  
 501 reflected by the particle bed is less than 1% of  $En_{in}$  and 13% is reflected by the wall. This difference  
 502 is due to the absorptivity of SiC (almost black) that is considerably higher than the one of the kiln  
 503 wall (almost white, see tables B1 and B2). The presence of SiC reduces the reflections inside the cavity  
 504 and furthermore, the particles cover partially the crucible, reducing the wall area that faces the kiln  
 505 aperture. In P1 and P3, radiation losses from the crucible wall are respectively 5.9% and 6.7% of  $En_{in}$ .  
 506 Radiation losses from the bed arise to almost 4% in the third step.

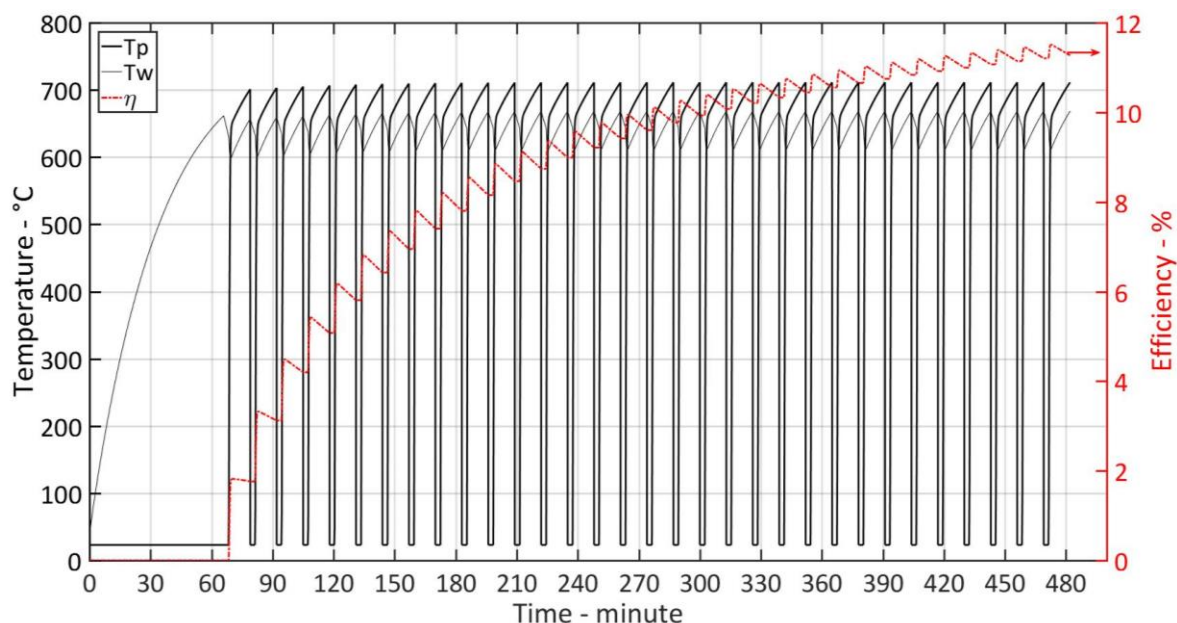
507 UARR efficiency is calculated following equation 12. It is evaluated at each time step and  
 508 reached a maximum efficiency of 0.85% at the beginning of P3, and a value of 0.65% at the end of P3.  
 509 This low efficiency is justified because most of the energy is used to heat up the UARR components  
 510 (cavity, insulations, steel rotor, casing, etc.) during the preheating step and only one load of particles  
 511 was realized in the trial. Moreover, the receiver mass is approximately two orders of magnitude  
 512 higher than the mass of the particle bed. However, these values are in agreement with results  
 513 reported for trials realized in reactors that worked in batch mode (0.45 – 3.1% according to Tescari et  
 514 al. (2013), Alonso et al. (2017b) and Schunk et al. (2009). Nevertheless, in an industrial scale, a kiln  
 515 that works in batch mode should be operated to carry out fast loading and unloading phases in order  
 516 to reduce the furnace cooling. Therefore, to reduce the supplied energy and to increase the efficiency,  
 517 initial preheating should be performed just once, and then, several particle charges and discharges  
 518 could be executed. In the case of UARR, another factor that penalizes the results are reflection losses  
 519 that are considerable high due to the reflectivity of the alumina, and to the relatively large kiln  
 520 aperture, as mentioned above. Natural convective losses in the particle bed and inside the kiln are  
 521 also significant due to the great difference of temperature between particles/cavity and the  
 522 environment. On the contrary, forced convection results almost negligible, due to the low rotational  
 523 speed. Finally, conductive losses could be substantially reduced, improving the insulation of the  
 524 UARR cavity.

525 Furthermore, depending on the application, it should be interesting to remove the particles from  
 526 the cavity when a desired temperature is reached, before to get the steady state. In this way, a great  
 527 amount of energy should be saved, and the process efficiency improves considerably because the  
 528 particle temperature increases substantially in the first minutes after loading. Afterwards, the  
 529 temperature variation is marginal (see Fig. 6 and 7). An example of this operation mode is reported  
 530 in the following chapter.

531  
 532  
 533

## 535 4.3. Batch processing assessment

537 A likely use of the UARR for the treatment of several batches of granular material is proposed  
 538 and assessed. Depending on the desired material treatment, a setpoint temperature should be  
 539 defined. The empty kiln is preheated at the beginning of the process just once and then, particles are  
 540 introduced into the receiver until they reach the setpoint temperature. After that, they are unloaded,  
 541 and another batch is inserted into the kiln cavity. The procedure is repeated several times. An  
 542 example of this operating mode is shown in Fig. 11. In that case, the setpoint temperature is 700 °C  
 543 and thirty-two batches of 43 g of silicon carbide are introduced and discharged every 13 minutes.  
 544 During a working period of 8 hours, 1.38 kg of material can be treated. As can be observed, the  
 545 efficiency increases during all the process and reaches a value close to the 12%.  
 546



547 Fig. 11. Particle temperature ( $T_p$ ), wall temperature ( $T_w$ ), and UARR efficiency ( $\eta$ ) for a setpoint  
 548 temperature of 700 °C.  
 549  
 550

551 An analogous assessment is realized for setpoint temperatures of 600, and 800 °C. In Fig. 12, the  
 552 UARR efficiencies are indicated for different working periods. As can be seen, the higher the working  
 553 period the higher the efficiency, and the lower the setpoint the higher the efficiency. In the case of the  
 554 setpoint fixed to 600 °C, fifty-seven batches and 2.45 kg of SiC can be treated for eight hours. This is  
 555 possible because the time to reach the desired temperature (treatment time) is shorter and it takes  
 556 approximately eight minutes. For this case, a maximum UARR efficiency of more than 20% is  
 557 estimated. Table 4 summarizes the results and the parameters used in the simulations.

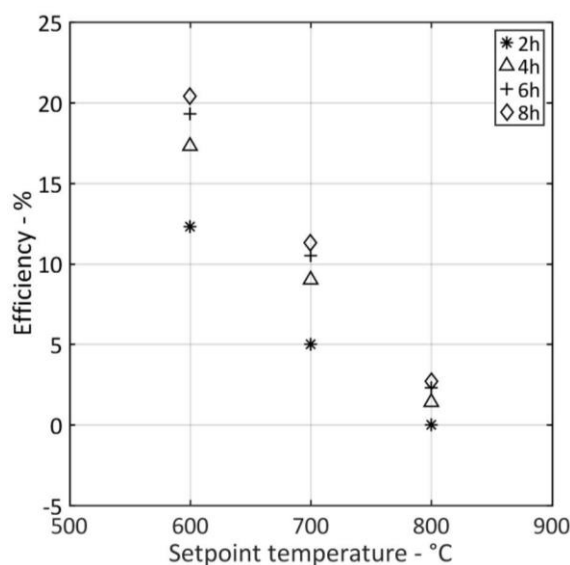


Fig. 12. UARR efficiency for different setpoint temperatures and working hours.

558  
559  
560

561  
562

Table 4. Mass and batches treated for different working time (2, 4, 6, 8 hours) and for different setpoint temperatures (SPT). Treating time and pre-heating (PH) time are also indicated.

| SPT<br>(°C) | Treating<br>time<br>(minute) | PH time<br>(minute) | 2 hr         |              | 4 hr         |              | 6 hr         |              | 8 hr         |              |
|-------------|------------------------------|---------------------|--------------|--------------|--------------|--------------|--------------|--------------|--------------|--------------|
|             |                              |                     | batch<br>(-) | mass<br>(kg) | batch<br>(-) | mass<br>(kg) | batch<br>(-) | mass<br>(kg) | batch<br>(-) | mass<br>(kg) |
| 600         | 7.75                         | 43                  | 10           | 0.43         | 25           | 1.09         | 41           | 1.76         | 57           | 2.45         |
| 700         | 13                           | 66                  | 4            | 0.18         | 13           | 0.58         | 23           | 0.97         | 32           | 1.39         |
| 800         | 45                           | 140                 | 0            | 0.00         | 2            | 0.10         | 5            | 0.21         | 8            | 0.33         |

563

## 564 5. Conclusion

565 Solar rotary kilns are presented as an option for direct thermal treatment of particles and for  
566 production of industrial process heat. Moreover, they have the potential to be used in storage systems  
567 above the typical operation temperature range of molten salt (> 600 °C). In order to asses this  
568 technology, a lab scale solar rotary kiln (UARR) was tested to work in batch mode at LaCoSA of  
569 University of Antofagasta, using a 7-kW<sub>e</sub> High Flux Solar Simulator as concentrated radiation  
570 source. Silicon carbide was selected to provide information about thermal treatment of particles  
571 because it is inert, and used in several CSP researches as thermal “vector” and as thermal medium  
572 for heat storage systems.

573 The UARR was tested satisfactorily under different conditions (static, rotating, empty and filled).  
574 A steady state temperature of approximately 800 °C in the interior of the empty cavity was achieved  
575 after approximately 165 minutes. Then, the kiln was filled with 43 g of SiC particles and was heated  
576 again. In less than a couple of minutes, the SiC temperature overcame the crucible one; then, the  
577 steady state was reached 83 minutes after the particle loading, achieving a SiC temperature of 820 °C.

578 Results from a transient one-dimensional numerical model show a good agreement with the  
579 experimental measurement and a relative error is lower than 2.4% for more than 50% of the data and  
580 an error of 6% for 75% of the data. The numerical model is solved in a very short computational time,  
581 approximately three minutes, thanks to some applied simplifications: low Biot numbers allow to  
582 assume a uniform radial temperature in both the crucible wall and the particle bed, and average  
583 temperatures are considered in the kiln axial direction. However, in longer kilns, a three-dimensional  
584 analysis is recommended, due to the likely temperature gradients that can arise in the longitudinal  
585 direction.

586 The kiln efficiency results equal to almost 1% for the present experimental procedure. This value,  
 587 that is typical for single trial realized in receivers and reactors that work in batch mode, is justified  
 588 because most of the energy (60%) is used to preheat the empty kiln. Furthermore, due to the high  
 589 reflectivity of the alumina crucible and to the relatively large aperture of the kiln, a great amount of  
 590 energy (35% of inlet power) is reflected to the environment. In an industrial scale, a batch operating  
 591 mode should be planned to reduce the furnace cooling during the phases of material loading and  
 592 unloading. In this way, the initial preheating up to a defined temperature should be performed only  
 593 the first time, and then particles can be charged and discharged several times with a limited supply  
 594 of energy.

595 An example of the UARR operation in batch mode during up to 8h shows as the kiln could be  
 596 used for several batches of granular material with an increasing efficiency up to more than 20%.  
 597 Additionally, this work proves the suitability of a rotary solar receiver for different applications  
 598 involving direct heating of particles in a temperature range of 600-850 °C, with the potential to  
 599 operate with high efficiency. This detailed analysis is performed using the developed numerical  
 600 model and shows its applicability to the construction of further solar rotary kilns, their scaled up and  
 601 optimization for specific applications.

## 602 Acknowledgments

603 The authors acknowledge the financial support provided by the FONDECYT project number  
 604 3150026 of CONICYT (Chile), the Education Ministry of Chile Grant PMI ANT 1201, as well as  
 605 CONICYT/ FONDAP/ 15110019 “Solar Energy Research Center” SERC-Chile.

606 The authors also gratefully acknowledge the financial support received from the Sectorial Fund  
 607 CONACYT-SENER-Energy Sustainability, through grant 207450, Mexican Center for Innovation in  
 608 Solar Energy (CeMIE-Sol), within strategic project P-10 “Solar Fuels and Industrial Processes”  
 609 (COSOLpi).

610 Special thanks go to the students Lou Cardinale, Rodrigo Méndez, and Daniel Vidal who gave  
 611 a precious contribution during the experimental trials at LaCoSA of University of Antofagasta.

## 612 Appendix A. Geometrical data

613 With the working condition of the kiln used in the experiment ( $N=7.5$  rpm,  $FR\%=10.9\%$ ), the  
 614 volume occupied by the granular bed ( $V_b$ ) could be approximated by a cylindrical segment ( $A_b^{tr} \cdot L$ ).  
 615 In equations A1-A6,  $V_{cav}$  is the inner volume of the cavity,  $\theta$  is the center angle that is delimited by  
 616 the bed chord  $c$  (see equation A2 and Fig. 1b),  $h$  is the constant height of the bed, and  $A_{cb-cw}$  is the  
 617 contact surface between the bed and the inner surface of the crucible.

$$FR\% = \frac{V_b}{V_{cav}} \cdot 100 \quad (A1)$$

$$A_b^{tr} = \frac{V_b}{L} = \frac{R^2(\theta - \sin \theta)}{2} \quad (A2)$$

$$c = 2R \sin \frac{\theta}{2} \quad (A3)$$

$$A_b = c \cdot L \quad (A4)$$

$$h = R \left( 1 - \cos \frac{\theta}{2} \right) \quad (A5)$$

$$A_{cb-cw} = \theta \cdot R \cdot L + 2A_b^{tr} \quad (A6)$$

## 618 Appendix B. Particle properties

619 The properties of particles and kiln components are resumed in table B1 and B2.

620 Table B1. Silicon carbide particle properties (Gallo et al., 2015; Industrial Comercial Chile Ltda., 2018;  
621 Perry, 1997; Touloukian, 1967).

| Property               | Symbol          | Value             | Unit of measure    |
|------------------------|-----------------|-------------------|--------------------|
| bulk mass              | $m_b$           | 0.043             | kg                 |
| mean particle diameter | $D_p$           | $4 \cdot 10^{-4}$ | m                  |
| particle density       | $\rho_p$        | 3215              | $\text{kg m}^{-3}$ |
| bulk density           | $\rho_b$        | 1720              | $\text{kg m}^{-3}$ |
| emissivity             | $\varepsilon_p$ | 0.85              | -                  |

622 Table B2. UARR properties as function of temperature (Bellan et al., 2013a; Bentz and Prasad, 2007; Bogaard et  
623 al., 1993; Perry, 1997; Rath, 2019; Sweet et al., 1987; Touloukian, 1967).

| Property  | Unit                            |
|---|---------------------------------|
| $K_w = 29, 12, 9$ at 20, 500, 1000 °C   | $\text{W m}^{-1}\text{K}^{-1}$  |
| $cp_w = 1000 \cdot (1.0446 + 1.742 \cdot 10^{-4} \cdot T - 2.796 \cdot 10^{-4} \cdot T^{-2})$   | $\text{J kg}^{-1}\text{K}^{-1}$ |
| $\rho_w = 3900$   | $\text{kg m}^{-3}$              |
| $\varepsilon_w = 0.07$  | -                               |
| $K_{ins} = 0.06, 0.1, 0.16, 0.25, 0.39$ at 200, 400, 600, 800, 1000 °C  | $\text{W m}^{-1}\text{K}^{-1}$  |
| $cp_{ins} = 880, 1047$ at 200, 982 °C   | $\text{J kg}^{-1}\text{K}^{-1}$ |
| $\rho_{ins} = 100$  | $\text{kg m}^{-3}$              |
| $K_{steel} = 9.705 + 0.0176 \cdot T - 1.60 \cdot 10^{-6} \cdot T^2$   | $\text{W m}^{-1}\text{K}^{-1}$  |
| $cp_{steel} = 6.683 + 0.04906 \cdot T + 80.74 \cdot \log(T)$  | $\text{J kg}^{-1}\text{K}^{-1}$ |
| $\rho_{steel} = 7750$   | $\text{kg m}^{-3}$              |
| $\varepsilon_{steel} = 0.07$  | -                               |
| $K_p = 1299 - 3.9407 \cdot T + 4.8745 \cdot 10^{-3} \cdot T^2 - 2.6974 \cdot 10^{-6} \cdot T^3 + 5.4787 \cdot 10^{-10} \cdot T^4$   | $\text{W m}^{-1}\text{K}^{-1}$  |
| $cp_p = -126.97 + 3.7396 \cdot T - 4.1047 \cdot 10^{-3} \cdot T^2 + 2.1063 \cdot 10^{-6} \cdot T^3 - 4.0566 \cdot 10^{-10} \cdot T^4$   | $\text{J kg}^{-1}\text{K}^{-1}$ |
| $K_{air} = 1299 - 3.9407 \cdot T + 4.8745 \cdot 10^{-3} \cdot T^2 - 2.6974 \cdot 10^{-6} \cdot T^3 + 5.4787 \cdot 10^{-10} \cdot T^4$   | $\text{W m}^{-1}\text{K}^{-1}$  |
| $cp_{air} = 997.6 + 1.458 \cdot 10^{-1} \cdot T - 1.236 \cdot 10^{-3} \cdot T^2 + 4.085 \cdot 10^{-6} \cdot T^3 - 5.371 \cdot 10^{-9} \cdot T^4 + 3.526 \cdot 10^{-12} \cdot T^5 - 1.159 \cdot 10^{-15} \cdot T^6 + 1.523 \cdot 10^{-19} \cdot T^7$ | $\text{J kg}^{-1}\text{K}^{-1}$ |

624

## 625 Appendix C. Thermal model

626 In the UARR the incoming radiation from the solar simulator is transferred by radiation,  
627 reflection, convection and conduction to the kiln component and to the particle bed. Hereunder, these  
628 mechanisms are detailed.

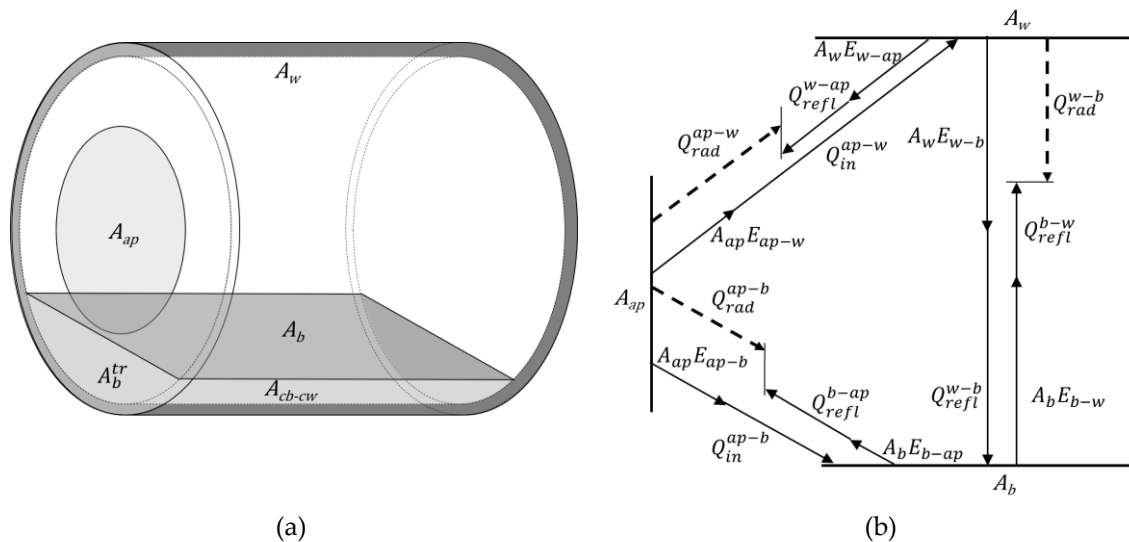
### 629 C.1. Radiative heat transfer

630 Radiative losses ( $Q_{rad}^l$ ) calculation in cavity receivers are often challenging. Due to the geometry  
631 complexity and thermal gradients inside the cavity, some geometry simplifications are assumed to  
632 calculate surface view factors ( $F_{x-y}$ ). For each material surface the temperature is considered spatially  
633 uniform as well as its emissivity, absorptivity, and reflectivity. Cases with and without particles  
634 inside the kiln are distinguished. For the case without particles, two surfaces are considered: aperture  
635 ( $A_{ap}$ ) and interior cavity wall ( $A_w$ ).  $F_{ap-w}$  is assumed equal to 1 because aperture is a flat surface  
636 facing the inner walls of the cavity.  $F_{w-ap}$  is calculated as the ratio between both surfaces:  $A_{ap}/A_w$ .

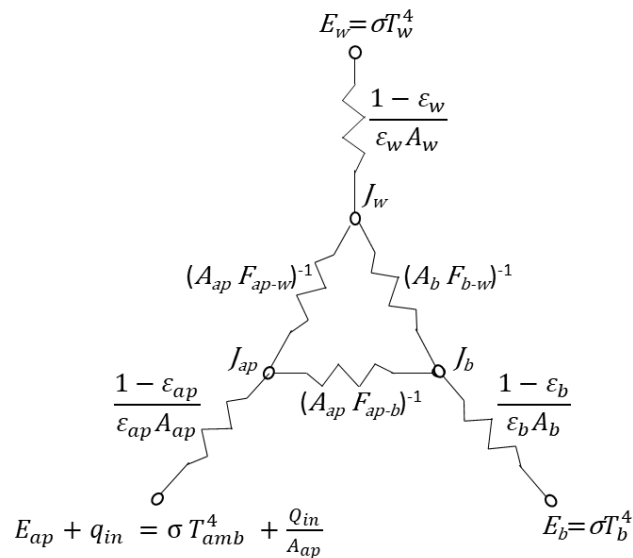
637 For cases with particles, the upper particle bed surface ( $A_b$ ) is treated as a plane that cuts the  
638 cylinder volume. In these cases,  $A_w$  represents the part of an interior cavity wall that is not covered  
639 by particles. A radiation network approach applied to a three-surface enclosure is adopted (see Fig.  
640 C1 and C2).

641 In Fig. C1b, a schematic diagram of the radiative exchange is depicted and in Fig. 6, the  
642 triangular configuration of the radiation network is shown. The radiation network is based on an  
643 analogy with an electrical system where resistances are  $(A_i \cdot F_{ij})^{-1}$  and the differences of radiosity of

644 each surface ( $J_i - J_j$ ) or ( $E_i - J_j$ ) are the driving potentials (Incropera et al., 2011a). The generic radiosity  
 645  $J_i$  is defined as the sum of the emitted and reflected radiative flux by the  $i$ -surface, while  $E_i$  represents  
 646 the total emissive power of a blackbody at the temperature of the  $i$ -surface. For the aperture, the  
 647 entering radiative flux is considered equal to the sum of the emissive power of the environment ( $E_{ap}$ )  
 648 and the heat flux on the aperture surface ( $q_{in}$ ). Each effective radiative exchange  $Q_{rad}^{i-j}$ , indicated in  
 649 Fig. 6, is obtained multiplying the radiosity difference for the area  $A_i$  of the  $i$ -surface and the  
 650 corresponding view factor  $F_{ij}$ . In the case of the aperture, reflections are not considered, and the  
 651 emitted power corresponds to the incoming solar power  $Q_{in}$ .  $Q_{in}$  is split into two components, one  
 652 towards the inner cavity and another one towards the particle bed.



653 Fig. C1. (a) Cavity surfaces considered in the model. (b) radiative exchanges between surfaces. Arrow  
 654 directions represent positive values during receiver heating ( $Q_{in} > 0$ ).



655  
 656 Fig. C2. Radiation network approach for three-surface enclosure applied to the rotary kiln (Incropera et al.,  
 657 2011a).

658  
 659 View factor calculation of each surface pair (see Fig. C2) is based on the reciprocity relations ( $A_i F_{i-j} =$   
 660  $A_j F_{j-i}$ ) and the summation rule ( $\sum_{j=1}^n F_{i-j} = 1$ ).  $F_{b-ap}$  is based on the correlation proposed by Abishek  
 661 et al. (2007) for the case of a disk and a rectangle in perpendicular planes (see equation C1.1). The  
 662 disk represents the cavity aperture and the rectangle corresponds to the plane cutting the cylinder  
 663 just below the aperture without any gap between them. Therefore, this method neglects the gap

664 between the particle bed and the aperture (see Fig. C1a). The following correlation is valid for 0.1 <  
 665  $\frac{L}{R_{ap}} < 10.0$  and  $0.1 < \frac{c}{R_{ap}} < 10.0$ .

$$F_{b-ap} = \frac{0.5974 \left[ \left( 0.05 \frac{c}{R_{ap}} + \left( \frac{c}{R_{ap}} \right)^2 \right)^{0.4976} \left( 0.05 \frac{L}{R_{ap}} + \left( \frac{L}{R_{ap}} \right)^2 \right)^{0.2091} + 0.5974 (0.1 A_{ap} + A_{ap}^2)^{0.0613} \right]}{\left( \frac{c}{R_{ap}} + \left( \frac{c}{R_{ap}} \right)^4 \right)^{0.4685} + \left( \frac{L}{R_{ap}} + \left( \frac{L}{R_{ap}} \right)^4 \right)^{0.30775} + (A_{ap} + A_{ap}^2)^{0.7457}} \quad (C1.1)$$

666 Once all the  $F_{i-j}$  are known, a lineal system is solved to estimate the radiosities in each node  
 667 (Incropera et al., 2011a). The system is written with the use of a matrix in the following form:

$$[\mathbf{A}] \cdot [\mathbf{J}] = [\mathbf{B}] \quad (C1.2)$$

668 where,

$$[\mathbf{A}] = \begin{pmatrix} F_{w-ap} + F_{w-b} + \frac{\varepsilon_w}{1 - \varepsilon_w} & -F_{w-b} & -F_{w-ap} \\ -F_{b-w} & F_{b-ap} + F_{b-w} + \frac{\varepsilon_b}{1 - \varepsilon_b} & -F_{b-ap} \\ 0 & 0 & 1 \end{pmatrix} \quad (C1.3)$$

$$[\mathbf{J}] = \begin{pmatrix} J_w \\ J_b \\ J_{ap} \end{pmatrix} \quad (C1.4)$$

$$[\mathbf{B}] = \begin{pmatrix} \sigma T_w^4 \frac{\varepsilon_w}{1 - \varepsilon_w} \\ \sigma T_b^4 \frac{\varepsilon_b}{1 - \varepsilon_b} \\ \sigma T_{amb}^4 + \frac{Q_{in}}{A_{ap}} \end{pmatrix} \quad (C1.5)$$

669 and it is solved for  $[\mathbf{J}]$  using the expression of equation C1.6.

$$[\mathbf{J}] = [\mathbf{A}]^{-1} [\mathbf{B}] \quad (C1.6)$$

670 Because  $\varepsilon_{ap} = 1$ , the third coefficient row of  $[\mathbf{A}]$  can be simplified and  $J_{ap}$  results equal to  $E_{ap} +$   
 671  $q_{in}$ , as in a short circuit, where no resistances are present. However, radiosities depend on surface  
 672 temperature, hence the system is solved for each time step at which the balance of energy is  
 673 computed. The total radiative exchange between each pair of surfaces can be counted as indicated in  
 674 equations C1.7, C1.8, and C1.9.

$$Q_{rad}^{w-b} = -Q_{rad}^{b-w} = A_w F_{w-b} (J_w - J_b) = A_b F_{b-w} (J_b - J_w) \quad (C1.7)$$

$$Q_{rad}^{b-ap} = -Q_{rad}^{ap-b} = A_b F_{b-ap} (J_b - J_{ap}) = A_{ap} F_{ap-b} (J_{ap} - J_b) \quad (C1.8)$$

$$Q_{rad}^{w-ap} = -Q_{rad}^{ap-w} = A_w F_{w-ap} (J_w - J_{ap}) = A_{ap} F_{ap-w} (J_{ap} - J_w) \quad (C1.9)$$

675 Finally, equation C1.10 quantifies the receiver radiation losses through the kiln aperture due to  
 676 the temperature difference between wall or particles and the external environment.

$$Q_{rad}^l = Q_{rad-out}^w + Q_{rad-out}^b = A_w E_{w-ap} + A_b E_{b-ap} = \frac{\sigma (T_w^4 - T_{amb}^4) A_w}{\frac{1}{F_{w-ap}} + \frac{1 - \varepsilon_w}{\varepsilon_w}} + \frac{\sigma (T_b^4 - T_{amb}^4) A_b}{\frac{1}{F_{b-ap}} + \frac{1 - \varepsilon_b}{\varepsilon_b}} \quad (C1.10)$$

## 677 B.2. Reflection losses

678 Cavity receivers present lower reflection losses than external ones; however, part of the radiation  
 679 impinging on the receiver is still reflected towards the environment from the particles and kiln wall.

680 From Fig. C1b and C2 equations C2.1-C2.3 can be deduced and used to quantify the reflection losses  
681 in the model.

$$Q_{refl}^{w-ap} = A_{ap}E_{ap-w} + Q_{in}^{ap-w} - Q_{rad}^{w-ap} - Q_{rad-out}^w = J_{ap}A_{ap}F_{ap-w} - Q_{rad}^{w-ap} - Q_{rad-out}^w \quad (C2.1)$$

$$Q_{refl}^{b-ap} = A_{ap}E_{ap-b} + Q_{in}^{ap-b} - Q_{rad}^{b-ap} - Q_{rad-out}^b = J_{ap}A_{ap}F_{ap-b} - Q_{rad}^{b-ap} - Q_{rad-out}^b \quad (C2.2)$$

$$Q_{refl}^l = Q_{refl}^{w-ap} + Q_{refl}^{b-ap} \quad (C2.3)$$

682 *B.3. Convective losses*

683

$$h_{cv} = h_{nc} + h_{fc} = \frac{Nu_{nc} \cdot K_{air}}{D} + h_{fc} \quad (C3.1)$$

684 Stine and Mcdonald indicated that  $Nu$  for natural convection can be calculated by equations C3.2-  
685 C3.5, where  $Gr$  is the number of Grashof ( $10^5 < Gr < 10^{12}$ ),  $s$  is the slope of the reactor in degree (for the  
686 present case  $s = 0$ ),  $\beta$  the coefficient of volumetric expansion,  $\nu$  the cinematic viscosity of the air at  
687 the ambient temperature, and  $g$  is the gravity acceleration (Mcdonald, 1995),

$$Nu_{nc} = 0.088 \cdot Gr^{\frac{1}{3}} \cdot \left(\frac{T_{cav}}{T_{amb}}\right)^{0.18} \cdot (\cos s)^{2.47} \cdot \left(\frac{D_{ap}}{D}\right)^p \quad (C3.2)$$

$$Gr = \frac{g \cdot \beta \cdot (T_{cav} - T_{amb}) \cdot D^3}{\nu^2} \quad (C3.3)$$

$$p = 1.12 - 0.982 \cdot \left(\frac{D_{ap}}{D}\right) \quad (C3.4)$$

$$T_{cav} = \frac{T_w A_w + T_b A_b}{A_{cav}} \quad (C3.5)$$

688 with  $A_{cav} = A_w + A_b$ . To calculate  $Nu$  for forced convection, the correlation in C3.6 from Ma (1993) is  
689 used,

$$h_{fc} = 0.1967 \cdot (v_{rot} + v_{air})^{0.1849} \quad (C3.6)$$

690 where  $v_{rot}$  and  $v_{air}$  are the kiln rotational speed and the air velocity in the room in  $m \cdot s^{-1}$ .

691 *B.4. Conduction losses*

692 As mentioned in the text, several models contact exchange coefficients have been proposed in  
693 literature. Here, it is shown the Li et al. (see equation C4.1 and C4.2) model that is the one that best  
694 fit with the experimental results.  $K_b$  is the effective bulk conductivity,  $\varphi$  is the bed porosity, and  $\alpha_b$   
695 is the thermal diffusivity.

$$Q_{cd}^{w-b} = -Q_{cd}^{b-w} = h_{w-b} A_{cb-cw} (T_w - T_b) \quad (C4.1)$$

$$h_{w-b} = \frac{1}{\frac{d_p \Gamma}{K_{air}} + \frac{1}{\frac{2K_b}{\sqrt{\pi \alpha_b}}}} \quad (C4.2)$$

$$K_b = \frac{1}{4} K_{air} \left\{ \frac{(2-3\varphi) \cdot K_p}{K_{air}} + 3\varphi - 1 + \sqrt{\left[ \left( \frac{(2-3\varphi) \cdot K_p}{K_{air}} \right) + 3\varphi - 1 \right]^2 + \frac{8K_p}{K_{air}}} \right\} \quad (C4.3)$$

$$\varphi = 1 - \rho_{rel} = 1 - \frac{\rho_b}{\rho_p} \quad (C4.4)$$

$$\alpha_b = \frac{K_b}{\rho_b \cdot cp_b} \quad (C4.5)$$

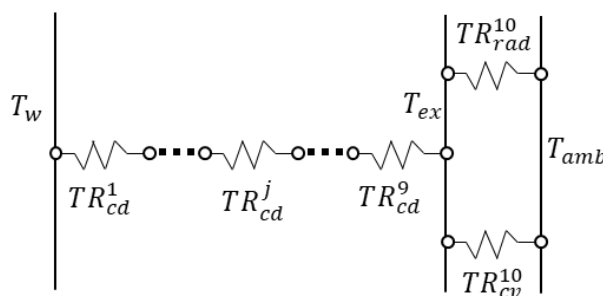
$$cp_b = \varphi \cdot cp_{air} + (1 - \varphi) \cdot cp_p \quad (C4.6)$$

696  $\rho_b$  and  $cp_b$  are the density and the specific heat of the particle bed, respectively.  $K_{air}$  and  $cp_{air}$  are  
 697 calculated at interstitial air temperature that is considered equal to bed temperature.  $\Gamma$  is a parameter  
 698 that is included between 0.096 and 0.198. Equations C4.3 corresponds to the EMT equation for the  
 699 effective conductivity.

#### 700 B.5. Insulation, rotor and casing heat losses

701 To quantify the heat losses due to conduction, radiation and convection from the receiver  
 702 external casing ( $Q_{ext}^l$ ), the UARR is discretized in the radial direction into five control volumes and  
 703 ten elements. Control volumes correspond to the different material layers. The external metal of the  
 704 case is split into two control volumes, and each control volume, except the last one, is subdivided  
 705 into two elements. An extra element is added to count the thermal exchange with the environment  
 706 (see Fig. C3). For sake of simplicity, bottom and front parts were considered adiabatic and rotation is  
 707 neglected in the conduction calculation.

708



709

710 Fig. C3. Electric circuit analogy for external heat losses from cavity wall to ambient around receiver external  
 711 casing.

712

713 Making the analogy with an electric system (see Fig. C3), thermal resistance due to conduction  
 714 ( $TR_{cd}$ ), convection ( $TR_{cv}$ ) and radiation ( $TR_{rad}$ ) can be calculated assuming a series and parallel  
 715 resistive circuit (Incropera et al., 2011b).

716 Thermal resistance by conduction through the different layers of the kiln shell is calculated  
 717 following the typical equation of a finite annular cylinder. For the elements  $1 < j < 9$ ,

$$TR_j = \frac{\ln(R_j/R_{j-1})}{2\pi K_j \cdot \Delta R_j} \quad (C5.1)$$

718 where  $R_j$ ,  $R_{j-1}$  and  $K_j$  are the inner radius, the external one and the conductivity of the  $j$  element.  $\Delta R_j$   
 719 is the length of the cylindrical element  $j$ . For the last element ( $j = 10$ ), thermal resistance is due to  
 720 external convection and radiation.

721

Hence, for the element  $j = 10$ ,

$$TR_{10} = TR_{rad-cv} = \frac{TR_{rad} \cdot TR_{cv}}{TR_{rad} + TR_{cv}} \quad (C5.2)$$

$$TR_{cv} = \frac{1}{h_{cv}^{ext} A_{ext}} \quad (C5.3)$$

$$TR_{rad} = \frac{1}{\varepsilon_{ext} \sigma A_{ext} (T_{ext} + T_{amb})(T_{ext}^2 + T_{amb}^2)} \quad (C5.4)$$

722 where  $T_{ext}$  and  $T_{amb}$  correspond to the external casing temperature and ambient temperature,  
 723 respectively.  $A_{ext}$ ,  $h_{cv}^{ext}$ ,  $\varepsilon_{ext}$  are the external surface, the convective coefficient and the emissivity of  
 724 the kiln casing. Note that  $A_{ext}$  represents only the lateral walls. This fact is justified by the presence  
 725 of higher thicknesses of insulation or stagnant air at the bottom and front parts of the UARR.  $\sigma$   
 726 is the Stefan-Boltzmann's constant.

727 The energy exchange in the receiver surfaces for a specific moment is reported so far; however,  
 728 to evaluate the receiver transient thermal behavior, it is also necessary to discretize the time. To solve  
 729 the heat losses due to conduction, a numerical explicit method is adopted, as it can be deduced from  
 730 the equations C5.5, C5.6 and C5.7.

731 The inner cavity wall temperature calculated in the transient model at the previous time step, is  
 732 used as boundary condition to estimate the temperature in radial direction of kiln insulations, rotor,  
 733 and casing. For  $i = 1$ ,

$$T_1^t = T_1^{t-1} + \frac{\Delta t}{m_1 \cdot cp_1} \cdot \left[ \frac{T_w^{t-1} - T_1^{t-1}}{TR_1} + \frac{T_1^{t-1} - T_2^{t-1}}{TR_2 + TR_3} \right] \quad (C5.5)$$

734 for the control volumes  $2 < i < 4$  and the elements  $j = 2i$ ,

$$T_i^t = T_i^{t-1} + \frac{\Delta t}{m_i \cdot cp_i} \cdot \left[ \frac{T_{i-1}^{t-1} - T_i^{t-1}}{TR_{j-2} + TR_{j-1}} + \frac{T_i^{t-1} - T_{i+1}^{t-1}}{TR_j + TR_{j+1}} \right] \quad (C5.6)$$

735 for  $i = 5$ ,  $T_5 = T_{ext}$ .

$$T_{ext}^t = T_{ext}^{t-1} + \frac{\Delta t}{m_5 \cdot cp_5} \cdot \left[ \frac{T_4^{t-1} - T_{ext}^{t-1}}{TR_8 + TR_9} + \frac{T_{ext}^{t-1} - T_{amb}^{t-1}}{TR_{10}} \right] \quad (C5.7)$$

736 To ensure the convergence, a stability criterium regarding the maximum time step is established  
 737 (see equation C5.8). Hence, the time step must be minor than a maximum value calculated for each  
 738 control volume ( $\Delta t < \Delta t_{max}^i$ ).

$$\frac{\Delta t_{max}^i}{m_i \cdot cp_i} \cdot \left[ \frac{T_{i-1}^{t-1} - T_i^{t-1}}{TR_{j-2} + TR_{j-1}} + \frac{T_i^{t-1} - T_{i+1}^{t-1}}{TR_j + TR_{j+1}} \right] < 1 \quad (C5.8)$$

739 Once the time step and  $Q_{ext}^t$  are known, the described energy balances can be solved.  
 740

## 741 Appendix D. Assessment of uncertainty and errors

### 742 D.1. Uncertainties in the measurement

743 Temperature measurements were realized with k-type thermocouples and were repeated three  
 744 times ( $r = 3$ ). The mean values  $T_{exp,i}^t$  is calculated at each instant ( $t$ ) of the  $i$ -thermocouple. Then an  
 745 unbiased standard deviation ( $\sigma_{1,i}^t$ ) is associated to the mean value.

$$\sigma_{1,i}^t = \frac{|T_{sim,i}^t - T_{exp,i}^t|}{T_{exp,i}^t} \cdot 100 \quad (D1.1)$$

746 The accuracy of k-type thermocouples is 0.75% of measured temperature (see equation D1.2).  
 747 Combining both uncertainties, the total uncertainty ( $\sigma_i^t$ ) is indicated in equation D1.3.

$$\sigma_{2,i}^t = 0.0075 \cdot T_{exp,i}^t \quad (D1.2)$$

$$\sigma_i^t = \sqrt{\sigma_{1,i}^t{}^2 + \sigma_{2,i}^t{}^2} \quad (D1.3)$$

748 *D.2. Errors in the model*

749 In order to assess the model quality, the percentage of the absolute relative errors ( $E_{r\%T_i}^t$ )  
 750 between simulated and experimental temperature curves at each time step ( $t$ ) are calculated as  
 751 indicated in equation D2.1

$$E_{r\%i}^t = \frac{|T_{sim,i}^t - T_{exp,i}^t|}{T_{exp,i}^t} \cdot 100 \quad (D2.1)$$

752 where  $i$  refers to the measurement of a specific thermocouple. Then, all the  $E_{r\%T_i}^t$  are arranged in  
 753 ascending order for the estimation of the cumulative frequency of the relative errors.

754 For completeness, the root-mean-square error (RMSE) and the mean absolute percentage error  
 755 (MAPE) are also calculated:

$$MAPE_i = \frac{\sum_{t=1}^n E_{r\%i}^t}{n} \quad (D2.2)$$

$$RMSE_i = \sqrt{\frac{\sum_{t=1}^n (T_{sim,i}^t - T_{exp,i}^t)^2}{n}} \quad (D2.3)$$

756

757 **References**

- 758 Abanades, S., Charvin, P., Flamant, G., 2007. Design and simulation of a solar chemical reactor for the thermal  
 759 reduction of metal oxides: Case study of zinc oxide dissociation. *Chem. Eng. Sci.* 62, 6323–6333.  
 760 <https://doi.org/10.1016/j.ces.2007.07.042>
- 761 Abedini Najafabadi, H., Ozalp, N., 2018. Aperture size adjustment using model based adaptive control strategy  
 762 to regulate temperature in a solar receiver. *Sol. Energy* 159, 20–36.  
 763 <https://doi.org/10.1016/j.solener.2017.10.070>
- 764 Abishek, S., Ramanujam, K.S., Katte, S.S., 2007. View Factors between Disk/Rectangle and Rectangle in Parallel  
 765 and Perpendicular Planes. *J. Thermophys. Heat Transf.* 21, 236–239. <https://doi.org/10.2514/1.26851>
- 766 Abyzov, A.M., Goryunov, A. V., Shakhov, F.M., 2013. Effective thermal conductivity of disperse materials. I.  
 767 Compliance of common models with experimental data. *Int. J. Heat Mass Transf.* 67, 752–767.  
 768 <https://doi.org/10.1016/j.ijheatmasstransfer.2013.08.045>
- 769 Alexopoulos, S.O., Dersch, J., Roeb, M., Pitz-Paal, R., 2015. Simulation model for the transient process behaviour  
 770 of solar aluminium recycling in a rotary kiln. *Appl. Therm. Eng.* 78, 387–396.  
 771 <https://doi.org/10.1016/j.applthermaleng.2015.01.007>
- 772 Alonso, E., Gallo, A., Roldán, M.I., Pérez-Rábago, C.A., Fuentealba, E., 2017a. Use of rotary kilns for solar thermal  
 773 applications: Review of developed studies and analysis of their potential. *Sol. Energy* 144, 90–104.  
 774 <https://doi.org/10.1016/j.solener.2017.01.004>
- 775 Alonso, E., Pérez-Rábago, C.A., Licurgo, J., Fuentealba, E., Estrada, C.A., 2015. First experimental studies of solar  
 776 redox reactions of copper oxides for thermochemical energy storage. *Sol. Energy* 115, 297–305.  
 777 <https://doi.org/10.1016/j.solener.2015.03.005>
- 778 Alonso, E., Pérez-Rábago, C.A., Licurgo, J., Gallo, A., Fuentealba, E., Estrada, C.A., 2017b. Experimental aspects  
 779 of CuO reduction in solar-driven reactors: Comparative performance of a rotary kiln and a packed-bed.  
 780 *Renew. Energy* 105, 665–673. <https://doi.org/10.1016/j.renene.2017.01.011>
- 781 Alonso, E., Romero, M., 2015. Review of experimental investigation on directly irradiated particles solar reactors.  
 782 *Renew. Sustain. Energy Rev.* 41, 53–67. <https://doi.org/10.1016/j.rser.2014.08.027>
- 783 Bellan, S., Alonso, E., Gomez-Garcia, F., Perez-Rabago, C., Gonzalez-Aguilar, J., Romero, M., 2013a. Thermal  
 784 performance of lab-scale solar reactor designed for kinetics analysis at high radiation fluxes. *Chem. Eng.*

- 785 Sci. 101, 81–89. <https://doi.org/10.1016/j.ces.2013.06.033>
- 786 Bellan, S., Alonso, E., Gomez-Garcia, F., Pérez-Rábago, C.A., González-Aguilar, J., Romero, M., 2013b. Thermal  
787 performance of lab-scale solar reactor designed for kinetics analysis at high radiation fluxes. *Chem. Eng.*  
788 *Sci.* 101, 81–89. <https://doi.org/10.1016/j.ces.2013.06.033>
- 789 Bentz, D., Prasad, K., 2007. Thermal performance of fire resistive materials I. characterization with respect to  
790 thermal performance models NISTIR 740, 1–21.
- 791 Boateng, A.A., 2008. The Rotary Kiln Evolution and Phenomenon, in: *Rotary Kilns*. Elsevier Inc., pp. 1–14.  
792 <https://doi.org/http://dx.doi.org/10.1016/B978-075067877-3.50003-9>
- 793 Bogaard, R.H., Desai, P.D., Li, H.H., Ho, C.Y., 1993. Thermophysical properties of stainless steels. *Thermochim.*  
794 *Acta* 218, 373–393. [https://doi.org/10.1016/0040-6031\(93\)80437-F](https://doi.org/10.1016/0040-6031(93)80437-F)
- 795 Carson, J.K., Lovatt, S.J., Tanner, D.J., Cleland, A.C., 2005. Thermal conductivity bounds for isotropic, porous  
796 materials. *Int. J. Heat Mass Transf.* 48, 2150–2158.  
797 <https://doi.org/10.1016/J.IJHEATMASSTRANSFER.2004.12.032>
- 798 Cengel, Y.A., 2002. Transient Heat Conduction, in: *Heat Transfer - A Practical Approach*. McGraw-Hill Higher  
799 Education, pp. 209–264.
- 800 Funken, K.-H., Pohlmann, B., Lüpfer, E., Dominik, R., 1999. Application of concentrated solar radiation to high  
801 temperature detoxification and recycling processes of hazardous wastes. *Sol. Energy* 65, 25–31.  
802 [https://doi.org/10.1016/S0038-092X\(98\)00089-9](https://doi.org/10.1016/S0038-092X(98)00089-9)
- 803 Gallo, A., González-Camarillo, H., Roldán, M.I., Alonso, E., Pérez-Rábago, C., 2018. Thermal Behavior and Heat-  
804 Flux Distribution in a Solar Rotary Kiln, in: *AIP Conference Proceedings: SolarPaces 2017*. pp. 1–8.  
805 <https://doi.org/10.1063/1.5067157>
- 806 Gallo, A., Marzo, A., Fuentealba, E., Alonso, E., 2017. High flux solar simulators for concentrated solar thermal  
807 research: A review. *Renew. Sustain. Energy Rev.* 77, 1385–1402. <https://doi.org/10.1016/j.rser.2017.01.056>
- 808 Gallo, A., Spelling, J., Romero, M., González-Aguilar, J., 2015. Preliminary Design and Performance Analysis of  
809 a Multi-Megawatt Scale Dense Particle Suspension Receiver. *Energy Procedia* 69, 388–397.  
810 <https://doi.org/10.1016/j.egypro.2015.03.045>
- 811 Gomez-Garcia, F., González-Aguilar, J., Romero, M., 2011. Experimental 3D flux distribution of a 7 kWe-solar  
812 simulator, in: *SolarPaces Conference*. Granada, Spain.
- 813 Gómez, F., Gonzalez-aguilar, J., Romero, M., n.d. Experimental 3D flux distribution of a 7 kW e -solar simulator.
- 814 Herz, F., Mitov, I., Specht, E., Stanev, R., 2012. Influence of operational parameters and material properties on  
815 the contact heat transfer in rotary kilns. *Int. J. Heat Mass Transf.* 55.  
816 <https://doi.org/10.1016/j.ijheatmasstransfer.2012.08.022>
- 817 Ho, C.K., 2017. A new generation of solid particle and other high-performance receiver designs for concentrating  
818 solar thermal (CST) central tower systems, in: *Advances in Concentrating Solar Thermal Research and*  
819 *Technology*. Woodhead Publishing, pp. 107–128. <https://doi.org/10.1016/B978-0-08-100516-3.00006-X>
- 820 Ho, C.K., 2016. A review of high-temperature particle receivers for concentrating solar power. *Appl. Therm. Eng.*  
821 109, 958–969. <https://doi.org/10.1016/j.applthermaleng.2016.04.103>
- 822 Incropera, F.P., De Witt, D., Bergman, T.L., Lavine, A.S., 2011a. 13.2.2 Radiation Exchange Between Surfaces, in:  
823 *Fundamentals of Heat and Mass Transfer*. John Wiley & Sons, Inc., pp. 824–829.
- 824 Incropera, F.P., DeWitt, D.P., Bergman, T.L., Lavine, A.S., 2011b. *Fundamentals of Heat and Mass Transfer*.
- 825 Industrial Comercial Chile Ltda., 2018. Silicon Carbide Powder - Data Sheet.
- 826 Kaneko, H., Miura, T., Fuse, A., Ishihara, H., Taku, S., Fukuzumi, H., Naganuma, Y., Tamaura, Y., 2007. Rotary-  
827 Type Solar Reactor for Solar Hydrogen Production with Two-step Water Splitting Process. *Energy & Fuels*

- 828 21, 2287–2293. <https://doi.org/10.1021/ef060581z>
- 829 Koepf, E., Villasmil, W., Meier, A., 2016. Pilot-scale solar reactor operation and characterization for fuel  
830 production via the Zn/ZnO thermochemical cycle. *Appl. Energy* 165, 1004–1023.  
831 <https://doi.org/10.1016/j.apenergy.2015.12.106>
- 832 Krueger, K.R., 2012. Design and Characterization of a Concentrating Solar Simulator. Phd Thesis.
- 833 Li, S.-Q., Ma, L.-B., Wan, W., Yao, Q., 2005. A Mathematical Model of Heat Transfer in a Rotary Kiln Thermo-  
834 Reactor. *Chem. Eng. Technol.* 28, 1480–1489. <https://doi.org/10.1002/ceat.200500241>
- 835 Li, X., Kong, W., Wang, Z., Chang, C., Bai, F., 2010. Thermal model and thermodynamic performance of molten  
836 salt cavity receiver. *Renew. Energy* 35, 981–988. <https://doi.org/10.1016/j.renene.2009.11.017>
- 837 Ma, R.Y., 1993. Wind Effects on Convective Heat Loss From a Cavity Receiver for a Parabolic Concentrating  
838 Solar Collector.
- 839 Maxwell, J.C., 1873. *A Treatise on Electricity and Magnetism*. Oxford.
- 840 McDonald, C.G., 1995. Heat Loss from an Open Cavity.
- 841 Meier, A., Bonaldi, E., Cella, G.M., Lipiński, W., Wuillemain, D., 2006. Solar chemical reactor technology for  
842 industrial production of lime. *Sol. Energy* 80, 1355–1362. <https://doi.org/10.1016/j.solener.2005.05.017>
- 843 Meier, A., Bonaldi, E., Cella, G.M., Lipinski, W., Wuillemain, D., Palumbo, R., 2004. Design and experimental  
844 investigation of a horizontal rotary reactor for the solar thermal production of lime. *Energy* 29, 811–821.  
845 [https://doi.org/10.1016/S0360-5442\(03\)00187-7](https://doi.org/10.1016/S0360-5442(03)00187-7)
- 846 Mellmann, J., 2001. The transverse motion of solids in rotating cylinders—forms of motion and transition  
847 behavior. *Powder Technol.* 118, 251–270. [https://doi.org/10.1016/S0032-5910\(00\)00402-2](https://doi.org/10.1016/S0032-5910(00)00402-2)
- 848 Neises, M., Tescari, S., de Oliveira, L., Roeb, M., Sattler, C., Wong, B., 2012. Solar-heated rotary kiln for  
849 thermochemical energy storage. *Sol. Energy* 86, 3040–3048. <https://doi.org/10.1016/j.solener.2012.07.012>
- 850 Perry, R.H., 1997. *Perry's Chemical Engineers' Handbook*, 7th ed. McGraw-Hill, New York.
- 851 Rath, 2019. Altra - Polycrystalline Alumina Fiber Mat - Data Sheet.
- 852 Sammouda, H., Royere, C., Belghith, A., Maalej, M., 1999. Heat transfer in a rotating furnace of a solar sand-  
853 boiler at a 1000 kW thermal concentration system. *Renew. Energy* 17, 21–47. [https://doi.org/10.1016/S0960-1481\(98\)00037-8](https://doi.org/10.1016/S0960-1481(98)00037-8)
- 854
- 855 Sarwar, J., Georgakis, G., LaChance, R., Ozalp, N., 2014. Description and characterization of an adjustable flux  
856 solar simulator for solar thermal, thermochemical and photovoltaic applications. *Sol. Energy* 100, 179–194.  
857 <https://doi.org/10.1016/j.solener.2013.12.008>
- 858 Schlunder, E.U., Mollekopf, N., 1984. Vacuum contact drying of free flowing mechanically agitated particulate  
859 material. *Chem. Eng. Process.* 18, 93–111. [https://doi.org/10.1016/0255-2701\(86\)80012-5](https://doi.org/10.1016/0255-2701(86)80012-5)
- 860 Schunk, L.O., Lipiński, W., Steinfeld, A., 2009. Heat transfer model of a solar receiver-reactor for the thermal  
861 dissociation of ZnO—Experimental validation at 10kW and scale-up to 1MW. *Chem. Eng. J.* 150, 502–508.  
862 <https://doi.org/10.1016/j.cej.2009.03.012>
- 863 Schunk, L.O., Steinfeld, A., 2009. Kinetics of the Thermal Dissociation of ZnO Exposed to Concentrated Solar  
864 Irradiation Using a Solar-Driven Thermogravimeter in the 1800 – 2100 K Range. *AIChE J.* 2, 1497–1504.  
865 <https://doi.org/10.1002/aic>
- 866 Siebers, D.L., Kraabel, J.S., 1984. Estimating Convective Energy Losses From Solar Central Receivers. SANDIA  
867 Rep.
- 868 Sweet, J.N., Roth, E.P., Moss, M., 1987. Thermal conductivity of Inconel 718 and 304 stainless steel. *Int. J.*  
869 *Thermophys.* 8, 593–606. <https://doi.org/10.1007/BF00503645>
- 870 Tescari, S., Agrafiotis, C., Breuer, S., De Oliveira, L., Neises-Von Puttkamer, M., Roeb, M., Sattler, C., 2013a.

- 871 Thermochemical solar energy storage via redox oxides: Materials and reactor/heat exchanger concepts.  
872 Energy Procedia 49, 1034–1043. <https://doi.org/10.1016/j.egypro.2014.03.111>
- 873 Tescari, S., Neises, M., de Oliveira, L., Roeb, M., Sattler, C., Neveu, P., 2013b. Thermal model for the optimization  
874 of a solar rotary kiln to be used as high temperature thermochemical reactor. Sol. Energy 95, 279–289.  
875 <https://doi.org/10.1016/j.solener.2013.06.021>
- 876 Touloukian, Y.S., 1967. Thermophysical properties of high temperature solid materials. MacMillan Co., New  
877 York.
- 878 Tscheng, S.H., Watkinson, A.P., 1979. Convective Heat Transfer in a Rotary Kiln. Can. J. Chem. Eng. 57, 433–443.  
879 <https://doi.org/10.1002/cjce.5450570405>
- 880 Valencia, J.J., Quested, P.N., 2008. Thermophysical Properties, in: ASM Handbook. pp. 468–481.  
881 <https://doi.org/10.1361/asmhba0005240>
- 882 Wes, G.W.J., Drinkenburg, A.A.H., Stemerding, S., 1976. Heat transfer in a horizontal rotary drum reactor.  
883 Powder Technol. 13, 185–192. [https://doi.org/10.1016/0032-5910\(76\)85003-6](https://doi.org/10.1016/0032-5910(76)85003-6)  
884